JAMES | Journal of Advances in Modeling Earth Systems

RESEARCH ARTICLE
10.1029/2023MS003938

A Novel Gravity Wave Transport Parametrization for Global Chemistry Climate Models: Description and Validation

Maria-Vittoria Guarino[1,2], Chester S. Gardner[3], Wuhu Feng[1,4], Bernd Funke[5], Maya García-Comas[5], Manuel López-Puertas[5], Marcin M. Kupilas[1], Daniel R. Marsh[1], and John M. C. Plane[1]

[1]School of Chemistry, University of Leeds, Leeds, UK, [2]Earth System Physics, International Centre for Theoretical Physics, Trieste, Italy, [3]Department of Electrical and Computer Engineering, University of Illinois at Urbana–Champaign, Urbana, IL, USA, [4]National Centre for Atmospheric Science (NCAS), University of Leeds, Leeds, UK, [5]Instituto de Astrofísica de Andalucía, CSIC, Granada, Spain

Abstract The gravity wave drag parametrization of the Whole Atmosphere Community Climate Model (WACCM) has been modified to include the wave-driven atmospheric vertical mixing caused by propagating, non-breaking, gravity waves. The strength of this atmospheric mixing is represented in the model via the "effective wave diffusivity" coefficient (K_{wave}). Using K_{wave}, a new total dynamical diffusivity (K_{Dyn}) is defined. K_{Dyn} represents the vertical mixing of the atmosphere by both breaking (dissipating) and vertically propagating (non-dissipating) gravity waves. Here we show that, when the new diffusivity is used, the downward fluxes of Fe and Na between 80 and 100 km largely increase. Larger meteoric ablation injection rates of these metals (within a factor 2 of measurements) can now be used in WACCM, which produce Na and Fe layers in good agreement with lidar observations. Mesospheric CO_2 is also significantly impacted, with the largest CO_2 concentration increase occurring between 80 and 90 km, where model-observations agreement improves. However, in regions where the model overestimates CO_2 concentration, the new parametrization exacerbates the model bias. The mesospheric cooling simulated by the new parametrization, while needed, is currently too strong almost everywhere. The summer mesopause in both hemispheres becomes too cold by about 30 K compared to observations, but it shifts upward, partially correcting the WACCM low summer mesopause. Our results highlight the far-reaching implications and the necessity of representing vertically propagating non-breaking gravity waves in climate models. This novel method of modeling gravity waves contributes to growing evidence that it is time to move away from dissipative-only gravity wave parametrizations.

Plain Language Summary Atmospheric gravity waves are generated in the lowest layers (~bottom 10 km) of the atmosphere by processes such as weather systems and air masses interacting with the topography, and can propagate upward to ~120 km. In this work, the representation of atmospheric gravity waves in a state-of-the-art chemistry climate model, the Whole Atmosphere Community Climate Model (WACCM), has been updated. In the new model version, the mixing of the atmosphere caused by gravity waves that propagate upwards above 80 km and do not break is part of the total mixing of the atmosphere, which hitherto was considered to be caused by the turbulence created by gravity wave breaking. We show here that when this additional source of atmospheric mixing is taken into account, the WACCM model is better able to simulate the sodium and iron atom densities in the upper layers of the atmosphere (between ~80 and 100 km), created by the ablation of cosmic dust. Additionally, gravity waves significantly affect the representation of CO_2 mixing ratios and air temperature within the model. Our work is important because it shows that propagating gravity waves have non-negligible impacts on basic properties of the Earth's atmosphere such as temperature, winds, and chemical species like CO_2, and that the lack of their representation in current climate models needs to be addressed.

Key Points:

- A parametrization representing vertical mixing by non-breaking gravity waves has been implemented in a chemistry-climate model
- Mesospheric CO_2 and temperature are significantly impacted by the additional source of vertical mixing
- Wave-induced constituent transport largely reconciles the modeled mesospheric Na and Fe layers with the estimated meteoric injection rates

Supporting Information:

Supporting Information may be found in the online version of this article.

Correspondence to:

M.-V. Guarino,
mguarino@ictp.it

Citation:

Guarino, M.-V., Gardner, C. S., Feng, W., Funke, B., García-Comas, M., López-Puertas, M., et al. (2024). A novel gravity wave transport parametrization for global chemistry climate models: Description and validation. *Journal of Advances in Modeling Earth Systems*, *16*, e2023MS003938. https://doi.org/10.1029/2023MS003938

Received 25 JULY 2023
Accepted 2 APR 2024

Author Contributions:

Conceptualization: Maria-Vittoria Guarino, Chester S. Gardner, Wuhu Feng, Daniel R. Marsh, John M. C. Plane
Data curation: Maria-Vittoria Guarino, Wuhu Feng
Formal analysis: Maria-Vittoria Guarino, Marcin M. Kupilas
Funding acquisition: Chester S. Gardner, Wuhu Feng, Daniel R. Marsh, John M. C. Plane
Investigation: Maria-Vittoria Guarino, Chester S. Gardner, Marcin M. Kupilas

1. Introduction

Atmospheric gravity waves generated in the troposphere by various sources (convection, frontogenesis, orography, etc.) can propagate over large vertical distances to over 120 km, reaching the Mesosphere and Lower Thermosphere (MLT) region. The stratosphere, and mesosphere in particular, are profoundly influenced by gravity waves. Waves that reach these high atmospheric levels have considerably increased their amplitudes, and

Methodology: Maria-Vittoria Guarino, Chester S. Gardner, Wuhu Feng, Daniel R. Marsh, John M. C. Plane
Project administration: Chester S. Gardner, Wuhu Feng, Daniel R. Marsh, John M. C. Plane
Resources: Wuhu Feng, Bernd Funke, Maya García-Comas, Manuel López-Puertas, John M. C. Plane
Software: Maria-Vittoria Guarino, Wuhu Feng
Supervision: Chester S. Gardner, Wuhu Feng, Manuel López-Puertas, Daniel R. Marsh, John M. C. Plane
Validation: Maria-Vittoria Guarino
Visualization: Maria-Vittoria Guarino
Writing – original draft: Maria-Vittoria Guarino, Chester S. Gardner, Manuel López-Puertas, John M. C. Plane
Writing – review & editing: Maria-Vittoria Guarino, Chester S. Gardner, Wuhu Feng, Bernd Funke, Maya García-Comas, Manuel López-Puertas, Marcin M. Kupilas, Daniel R. Marsh, John M. C. Plane

their breaking has a dramatic impact on the temperature and wind climatologies of these regions of the atmosphere. Gravity waves are responsible for the mesospheric zonal mean zonal wind reversal and drive the pole-to-pole circulation at the mesopause. Because of this, mesospheric winds and temperatures can only be simulated by climate models when wave drag is included (Holton & Alexander, 2000; McLandress, 1997). Gravity waves also contribute to shaping the global distribution and the atmospheric concentration of species like CO_2, atomic oxygen, meteoric metals, and nitric oxide via wave-induced vertical transport between the thermosphere and the mesosphere (see e.g. Crutzen, 1970; Garcia et al., 2014; Lary, 1997; Plane, 2012; Plane et al., 2015; Shepherd et al., 2004; Smith et al., 2010; Ward, 1999).

Gravity waves are well known to influence the global atmospheric circulation by deposition of horizontal momentum when they break. This effect has been represented in numerical weather prediction and climate models since the pioneering work of McFarlane (1987), who introduced a first orographic wave drag parametrization into the Canadian Climate Centre general circulation ("low-top") model. Thanks to computational advances over time, climate models started to represent the upper levels of the atmosphere (beyond the lower stratosphere) and "high-top" models incorporating the wave drag and diffusion due to non-orographic and non-stationary gravity waves, based on the work of Lindzen (1981), Matsuno (1982), Weinstock (1982), and Holton (1982, 1983), were developed.

The majority of gravity wave drag parametrizations used by state-of-the-art models today employ the same approach as those developed in the early 1980s, where gravity wave effects are represented by dissipative processes only. This means that for a wave to have any impact on the atmosphere in which it is propagating it has to dissipate and, as follows from linear wave theory, deposit wave momentum into the mean flow. Parametrizations for gravity wave-induced transport of chemically active species have also been proposed (see e.g. Garcia & Solomon, 1985). This process occurs when the wave-induced fluctuations in temperature and species density modulate the chemical reaction rates. None of the parametrizations above represent the motion of fluid parcels under the influence of a spectrum of propagating, non-breaking, gravity waves which, as first shown by Walterscheid and Hocking (1991), can also have an impact on the background flow.

Weinstock (1990) considered the atmospheric mixing that arises from non-linear interactions among all the waves in the spectrum. Walterscheid and Hocking (1991) showed that a spectrum of vertically propagating, non-breaking gravity waves induces a cumulative Stokes drift of atmospheric parcels that varies spatially. Consequently, the parcels drift apart in a manner analogous to diffusion. They called this process Stokes diffusion. In the real atmosphere, the superimposition of multiple waves means that the non-linear wave-wave interactions and the combined Stokes drift, imparted by the full spectrum of waves, mixes the background atmosphere in a process analogous to diffusion which can be represented via a diffusivity coefficient.

Atmospheric mixing by non-breaking gravity waves has been studied by several authors (see e.g. Gardner, 2018; Gardner & Liu, 2010; Grygalashvyly et al., 2012; Hickey et al., 2000; Liu & Gardner, 2004, 2005; Walterscheid & Hocking, 1991) who, by modeling and by making observations, showed that heat and atmospheric constituents can be transported vertically by wave-related processes other than turbulent mixing. Yet this additional source of atmospheric mixing is currently not accounted for in chemistry climate models.

Perhaps the most compelling evidence of wave-driven transport are the vertical heat and constituent flux profiles measured directly with Na and Fe Doppler lidars (see e.g. Chu et al., 2022; Gardner & Liu, 2010; Huang et al., 2015; Liu & Gardner, 2005), which can measure simultaneously the vertical wind, temperature, Na density, and Fe density fluctuations induced by the waves in the upper atmosphere. These instruments could not resolve turbulence or Brownian motion, so the fluctuations they measured, and the resulting fluxes that were computed from the measurements, had to have arisen exclusively from non-breaking gravity waves, which could be resolved. In developing a model for meteoric Na and Fe, included in the Whole Atmosphere Community Climate Model (WACCM), Feng et al. (2013) and Marsh et al. (2013) found that the Meteoric Input Function (MIF) had to be divided by a factor of 5 and 3, respectively, in order for the WACCM model to match the Fe and Na densities measured by resonance lidars. This indicates that the vertical Fe and Na transport in the MLT, as modeled by a global model such as WACCM, is too slow by a factor of up to ∼5 and points to the need for including in models the vertical transport induced by small-scale (unresolved) gravity waves.

Finally, we note that the missing wave-induced vertical transport is expected to influence the mesospheric concentrations of species like CO_2, whose current representation in the WACCM model has been shown by Garcia et al. (2014) to be sensitive to the magnitude of the model's eddy diffusivity.

Gardner et al. (2019) developed a theory that allows the motions imparted by vertically propagating gravity waves to be represented by an "effective wave diffusivity" coefficient K_{wave}, and showed that it should be possible to incorporate constituent transport by non-breaking gravity waves in global chemistry climate models. In this paper, we present the first implementation of this new wave-driven constituent transport parametrization for the WACCM model. We discuss here the details of the code implementation and use Community Earth System Model version 2 (CESM2) simulations to investigate the impact of the parametrized, vertically propagating, non-breaking gravity waves on the concentrations of Fe, Na, and CO_2, and on the temperature structure of the MLT region.

In Section 2, we describe the theoretical formulation (2.1) and the code implementation (2.2) of the parametrization. In Section 3, we provide technical details on the numerical simulations (3.1) and the lidar and satellite observations used for model-observation comparisons (3.2). In Section 4, we discuss the simulation results by comparing a standard WACCM run (without wave-induced transport) with a run using the new parametrization; in Section 4.2 we present model-observation comparisons for Na and Fe, and in Section 4.4 the same is done for mesospheric CO_2 and temperature. In Section 5, we summarize the main conclusions of the study.

2. A Parametrization of Wave-Driven Constituent Transport

2.1. Theoretical Formulation

The theoretical basis of the new parametrization is described in Gardner (2018) and Gardner et al. (2019). Here we summarize the key points of those studies, and provide the relevant equations used in the parametrization. In particular, we present some minor changes between the equations used in the present study and those in Gardner et al. (2019); these were required during the phase of code implementation.

Dissipating and non-dissipating gravity waves contribute to vertical constituent transport through four distinct mechanisms: (a) advection associated with the Stokes drift imparted by the vertically propagating wave spectrum (Coy et al., 1986; Gardner, 2018; Walterscheid & Hocking, 1991), (b) atmospheric mixing by non-breaking waves (Gardner & Liu, 2010; Liu & Gardner, 2004, 2005), (c) eddy mixing by turbulence generated by breaking waves (e.g., Colegrove et al., 1965), and (d) chemical transport by waves and turbulence (Gardner, 2018; Gardner & Liu, 2016; Walterscheid & Schubert, 1989). To simplify the implementation, here we focus on the first three mechanisms. Note also that, hereinafter, we will refer to vertically propagating non-breaking gravity waves simply as 'vertically propagating waves'. Despite all waves in the model being assumed to propagate vertically, we use this terminology to make a distinction between waves that influence the background atmosphere when they dissipate (breaking waves) and waves that do that as they travel through the medium.

The vertical constituent flux $\left(\overline{w'\rho'_C}\right)$ is defined as the expected value (denoted by the overbar) of the product of the vertical wind (w') and constituent density $\left(\rho'_C\right)$ fluctuations. The computation of the total vertical constituent flux induced by waves, turbulence, and molecular diffusion is given by Gardner (2018). The result for chemically inert species is:

$$\overline{w'\rho_C'}|_{Total} = \bar{\rho}_C \frac{\overline{w'\rho_A'}}{\bar{\rho}_A} - \bar{\rho}_C\left(\frac{1}{\bar{\rho}_C}\frac{\partial\bar{\rho}_C}{\partial z} - \frac{1}{\bar{\rho}_A}\frac{\partial\bar{\rho}_A}{\partial z}\right)K_{Total} \simeq -\bar{\rho}_C\left(\frac{1}{\bar{\rho}_C}\frac{\partial\bar{\rho}_C}{\partial z} - \frac{1}{\bar{\rho}_A}\frac{\partial\bar{\rho}_A}{\partial z}\right)K_{Total} \quad (1)$$

where ρ_C is the species density, ρ_A is the atmospheric density, K_{Total} is the total atmospheric mixing due to propagating non-breaking gravity waves (K_{wave}), breaking gravity waves (K_{zz}), and molecular diffusion (K_{mole}):

$$K_{Total} = K_{wave} + \left(1 + \xi_{inst}\right)\left(K_{zz} + K_{mole}\right) \quad (2)$$

and ξ_{inst} is the instability parameter (ξ_{inst}):

$$\xi_{inst} = \frac{\mathrm{Var}\left(\partial T'/\partial z\right)}{\left(\Gamma_{ad} + \partial \bar{T}/\partial z\right)^2} \simeq \frac{\mathrm{Var}\left(\partial u'/z\right)}{N^2} = 1/Ri \tag{3}$$

where T is temperature, u is horizontal wind, $\Gamma_{ad} = g/C_p$ is the adiabatic lapse rate, g is the gravitational acceleration, $C_p = 1{,}003\ \mathrm{m^2\ K^{-1}\ s^{-2}}$ is the specific heat at constant pressure, and N is the Brunt-Väisälä frequency. The instability parameter is the normalized lapse rate fluctuation variance, which, for gravity wave perturbations, is approximately equal to the mean of the inverse Richardson number (Ri). This is a measure of the instability of the atmosphere through which the waves are propagating. Larger values correspond to a less stable atmosphere and for gravity waves ξ_{inst} is always less than 1. In the presence of waves, the eddy and molecular diffusion are enhanced by the factor $(1 + \xi_{inst})$ because the waves perturb the constituent mixing ratio (Gardner, 2018; Grygalashvyly et al., 2012; Hickey et al., 2000).

The first term on the r.h.s in Equation 1 is the advective flux associated with the vertical Stokes drift $\left(\overline{w'\rho_{A'}}/\bar{\rho}_A\right)$ induced by the waves. WACCM does not include the impact of Stokes drift induced by the unresolved, parametrized waves, so we may set the Stokes drift term due to these waves to zero. The second term is the total diffusive flux associated with atmospheric mixing by waves, turbulence, and the thermal motion of the atmospheric molecules. In particular, K_{zz} is the eddy diffusivity associated with turbulence, K_{wave} is the effective constituent diffusivity associated with atmospheric mixing by non-breaking gravity waves, and K_{mole} is the molecular diffusivity of constituent C.

We can define a total dynamical diffusivity K_{Dyn} that only includes contributions from breaking and vertically propagating, non-breaking, gravity waves:

$$K_{Dyn} = K_{wave} + \left(1 + \xi_{inst}\right) K_{zz}. \tag{4}$$

Note that K_{zz} in Equation 4 is computed by the WACCM gravity wave drag scheme whenever waves dissipate and the gravity wave wind tendencies are non zero.

As shown in Gardner et al. (2019), K_{wave} is related to the vertical Stokes drift velocity as follows:

$$K_{\mathrm{wave}} = \frac{g}{N^2}\frac{\overline{w'\rho_{A'}}}{\bar{\rho}_A} = -\frac{g}{N^2}\left(\frac{\overline{w'T'}}{\bar{T}} - \frac{\overline{w'p'}}{\bar{p}}\right) \tag{5}$$

$\overline{w'T'}$ is the vertical sensible heat flux induced by the gravity waves, and $\overline{w'p'}$ is the gravity wave energy flux, where p is the atmospheric pressure.

Although similar, it is important to note that K_{wave} is different from the thermal diffusivity (K_H), which is defined in terms of the vertical flux of potential temperature $\left(\overline{w'\theta'}\right)$. By applying Fick's first law of diffusion, we obtain:

$$K_H = -\left(\frac{\partial \bar{\theta}}{\partial z}\right)^{-1}\overline{w'\theta'} = -\frac{g}{N^2}\left(\frac{\overline{w'T'}}{\bar{T}} - \kappa\frac{\overline{w'p'}}{\bar{p}}\right) = -\frac{g}{N^2}\frac{\overline{w'T'}}{\bar{T}} + K_E \tag{6}$$

where $\theta = T\left(\frac{p_0}{p}\right)^{\kappa}$ is the potential temperature, $\kappa = R/C_p$, $R = 287\ \mathrm{m^2\ K^{-1}\ s^{-2}}$ is the gas constant for dry air, $p_0 = 1{,}000$ hPa is the reference pressure, and where for convenience we define K_E as the effective diffusivity associated with the gravity wave energy flux:

$$K_E = \frac{g}{N^2}\kappa\frac{\overline{w'p'}}{\bar{p}}. \tag{7}$$

K_H represents the diffusion of background temperature by gravity waves. Note that, in the current version of WACCM, constituents and temperature are diffused by the same diffusivity coefficient (i.e., K_{zz}). This is possible since the pressure fluctuations induced by turbulence are negligible, and thus the eddy diffusivities for heat and

constituents are both equal to K_{zz}. However, to model the additional impact of non-dissipating waves, we need to include the relevant diffusion coefficients. For wave-induced atmospheric mixing, the diffusivities for constituents (K_{wave}) and heat (K_H) are different.

We focus next on the computations of the K_{wave} and K_H terms. From Equations 5–7 we can see that K_{wave} can be expressed in terms of K_H:

$$K_{wave} = K_H + \left(\frac{C_p}{R} - 1\right) K_E. \tag{8}$$

K_H can be computed from the linearized convection(advection)-diffusion equation for heat transfer, and assuming that gravity wave fluctuations are in hydrostatic balance, that is, $\overline{(\partial\theta'/\partial x)^2} \ll \overline{(\partial\theta'/\partial z)^2}$. Gardner et al. (2019) gives the full derivation for K_H (Section 4, Equations 15–19) here we just show their final expression:

$$K_H \simeq (K_{zz} + K_{wave})\xi_{inst}. \tag{9}$$

Note that compared to Equation (17) of Gardner et al. (2019), K_{Dyn} has been replaced in Equation 9 by $(K_{zz} + K_{wave})$. This is a more consistent approach because the enhanced eddy diffusivity (i.e., $(1 + \xi_{inst})K_{zz}$ in Equation 4) applies to species transport rather than the transport of potential temperature.

Combining Equations 8 and 9 we obtain:

$$K_{wave} = \frac{1}{(1 - \xi_{inst})}\left[\xi_{inst}K_{zz} + \left(\frac{C_p}{R} - 1\right)K_E\right] \tag{10}$$

K_{wave} depends on the eddy diffusivity K_{zz}, K_E, and ξ_{inst}.

From Equation 3 we can see that, in principle, the instability parameter ξ_{inst} can be computed directly from the spectrum of parametrized gravity waves produced by WACCM. However, rather than computing $\mathrm{Var}(\partial T'/\partial z)$ using the T' spectrum provided by the WACCM parametrization, which has been tuned to produce the desired mean atmospheric state, and where the horizontal wavelength is fixed for all the waves in the spectrum (see Section 2.2), we use for the computations of K_E and ξ_{inst} a model for the vertical wave-number spectrum of T', based upon numerous observations made throughout the troposphere, stratosphere, and mesosphere in both hemispheres.

For K_E, we use the expression derived by Chu et al. (2022) in the appendix of their paper and given by their Equation 12:

$$K_E = \frac{g}{N^2}\kappa\frac{\overline{w'p'}}{\overline{p}} \simeq 8\sqrt{2}(1 - 2\alpha_{down})\frac{\Gamma_{ad}f}{\overline{T}}\left(1 - \frac{4}{3}\sqrt{\frac{f}{N}}\right)\left[\frac{\mathrm{Var}(T')}{(\Gamma_{ad} + \partial\overline{T}/\partial z)^2}\right]^{3/2} \tag{11}$$

where α_{down} is the fraction of gravity wave energy propagating downward and f is the inertial frequency. Although all the unresolved modeled waves propagate upward, waves can propagate downward if they are reflected from above, are ducted (e.g., Y. Yu & Hickey, 2007; Walterscheid & Hickey, 2009), or are secondary waves generated above by the breaking of primary waves (e.g., Becker & Vadas, 2018). Numerous observational studies have shown that α_{down} can vary over a relatively wide range (from ∼15% to 50%) depending on location, altitude, and season (see e.g., Gavrilov et al., 1996; Hu et al., 2002; Strelnikova et al., 2020; Wang et al., 2005). For this study we assume $\alpha_{down} = 33\%$, regardless of altitude, geographic location, or season.

For ξ_{inst}, the model for the vertical wave-number spectrum of T' is described in Appendix A and is used to express the instability parameter in terms of the temperature perturbation variance:

$$\xi_{inst} = \frac{\gamma}{4} + \frac{\gamma}{2}\ln\left[\frac{(2\pi)^2}{\gamma\lambda_b^2}\frac{\mathrm{Var}\left(T'\right)}{\left(\Gamma_{ad} + \partial\overline{T}/\partial z\right)^2} + \frac{1}{2}\right], \tag{12}$$

where λ_b is the vertical wavelength that marks the transition from waves to turbulence, and γ is a tunable parameter that is determined by comparing the measured temperature spectrum to the model. For the WACCM results presented here, $\lambda_b = 1$ km and $\gamma = 1/8$.

Equations 4 and 10–12 have been implemented in the WACCM model source code to compute the new total dynamical diffusivity K_{Dyn} at each model time-step and grid-point. In the following section we discuss the details of the code implementation.

2.2. Code Implementation

In the WACCM model, atmospheric gravity waves generated by three different sources, that is, orography, convection (deep and shallow), and frontogenesis are parametrized. For the representation of non-orographic gravity wave drag, WACCM uses a full spectrum of waves (Garcia et al., 2007; Richter et al., 2010). Independently of the wave source, the wave spectrum is specified over a range of phase speeds c (with a fixed wavelength, see below) that spans from $c = -80$ m/s to $c = +80$ m/s, discretized with a $\Delta c = 2.5$ m s^{-1} interval, for a total of 64 wave-numbers. Details on the spectral shape, amplitude, and conditions for when and how the spectrum is launched are given by Charron and Manzini (2002) and Beres et al. (2005), for frontally—and convectively—generated gravity waves, respectively. For mid-frequency gravity waves, for which rotational effects are negligible, the horizontal wavelength is assumed to be fixed and equal to 100 km. The wave source spectrum as specified above is tuned so that the model can simulate stratospheric wind reversals and mesopause temperatures consistently with observations (Garcia et al., 2007). Orographic gravity wave drag is the result of stationary waves ($c = 0$) that are launched by the sub-grid scale orography. In the WACCM gravity wave drag module, the horizontal wavelength for these waves is determined based on the standard deviation of the sub-grid orography.

For waves that have propagated to sufficiently high altitudes to become unstable, gravity wave drag is parametrized by enforcing the saturation condition derived by McFarlane (1987). Waves that have reached their critical level ($c = U$) are removed from the wave spectrum by setting their stress to zero. Within saturation regions, the wind tendencies associated with the dissipating waves are computed by evaluating the vertical divergence of the wave stress τ, following Lindzen (1981). Outside of saturation regions, and up to ∼100 km, τ is constant since waves do not dissipate, according to linear theory. Above 100 km in the thermosphere, molecular diffusion becomes important and τ is damped accordingly. The reader is referred to Appendix A of Garcia et al. (2007) for a detailed description of the WACCM gravity wave drag module.

In implementing the new parametrization, we take into account contributions from both orographic and non-orographic mid-frequency gravity waves. Although most of the orographic gravity waves dissipate lower down in the atmosphere and thus are not expected to be major contributors to the MLT dynamics, they have been observed to propagate into the MLT region, where they can break and deposit their momentum (see e.g. Eckermann et al. (2016); Kruse et al. (2022)).

Following the approach used in WACCM for the computation of the eddy diffusivity K_{zz}, we assume that waves excited by different sources are independent from each other, and thus their effect on the total wave effective diffusivity K_{wave} and total dynamical diffusivity K_{Dyn} is additive. This means that computations for K_{Dyn} are carried out separately for orographic, convective and frontal waves, and the final total dynamical diffusivity is simply the sum of these three diffusivities.

K_{wave} is a function of K_{zz}, the environmental lapse rate $\left(d\overline{T}/dz\right)$ and total variance of the gravity wave temperature perturbation (Var(T')) (according to Equations 10–12). K_{zz} is directly available within the model code. In order to compute the gravity wave temperature perturbations T', and thus Var(T'), the following is done at each dynamic time-step:

1. For each wave phase-speed c within the source spectra, the model-generated wave stress τ (Pa) is used to compute the absolute momentum flux MF_{abs} (m^{2}s^{-2}):

$$MF_{abs} = \frac{\tau(c,x,y,z)}{\rho_A(x,y,z)}. \quad (13)$$

2. The amplitude of the associated gravity wave temperature perturbation is then computed at each grid-point and vertical level using the dispersion relation for mid-frequency gravity waves (Ern et al., 2004):

$$T' = \sqrt{\frac{MF_{abs}}{\frac{1}{2}\frac{\lambda_z}{\lambda_h}\left(\frac{g}{N\overline{T}}\right)^2}}, \quad (14)$$

where λ_z is the vertical wavelength, λ_h is the horizontal wavelength equal to 100 km (see above), and $\overline{T}$ is the background atmospheric temperature.

3. The total temperature perturbation variance is finally computed by summing T' over all frequencies for waves with frequency ω comprised between the Brunt-Väisälä frequency N and the inertial frequency f:

$$\mathrm{Var}\left(T'\right) = \sum_{\omega>f}^{\omega<N} \frac{1}{2}\left(T'\right)^2. \quad (15)$$

Because the wave stress τ is defined at the model's grid-box interfaces, all the calculations above are also carried out at these model interfaces. For consistency, the environmental lapse rate is computed using the atmospheric temperature at the model's grid-box mid-points using central differences, so that the resulting $d\overline{T}/dz$ is defined at the model interfaces.

Computations for K_{wave} and K_{Dyn} are carried out only above the tropopause height (after waves have been generated and the source spectra have been defined within the troposphere), so the new parametrization is only active above 200 hPa (~12 km).

The new total dynamical diffusivity K_{Dyn} replaces the eddy diffusivity K_{zz} everywhere in the model code where K_{zz} is used. In regions of wave dissipation, the total mixing of the atmosphere is given by Equation 4. Here vertically propagating waves increase the total atmospheric mixing by (a) enhancing the eddy diffusivity by the $(1 + \xi_{inst})$ factor, which represents how propagating waves perturb the background atmosphere, and (b) by introducing a new diffusivity term (K_{wave}). In regions where waves do not break ($K_{zz} = 0$), $K_{Dyn} = K_{wave}$. Thus, in our parametrization the spectrum of vertically propagating waves influences the background atmosphere inside and outside of dissipation regions. This is a major difference with traditional dissipative-only gravity wave parametrizations.

Note that, as explained in Section 2.1, for propagating waves the heat (K_H) and constituents (K_{wave}) diffusivity coefficients are similar but different. The approach described above, and used in this first code implementation, is to use K_{Dyn} everywhere in the model code where K_{zz} is used, meaning that K_{Dyn} is used to diffuse both temperature and constituents. Hence, constituents are diffused properly but the diffusion of heat is excessive. The total thermal diffusivity is too large by the amount $\left[\left(\frac{C_p}{R} - 1\right)K_E + \xi_{inst}K_{zz}\right]$ which can be large in regions where the atmosphere is stable. The consequences of excessive thermal diffusion will be discussed later when evaluating the modeled temperature profiles (see Sections 4.3.3 and 5).

In order to make the model numerically stable we had to (a) introduce a diffusive damping for the wave amplitude, and (b) bound the maximum value that K_{Dyn} can attain within the model vertical column. These two constraints are described below.

2.2.1. Wave- and Turbulence-Induced Diffusive Damping

When the total temperature perturbation variance is computed directly from the WCCAM Reynolds stress profiles (via Equation 13 to 15) without applying any damping, the simulated values are much larger than the available measurements of Var(T') in the stratosphere and mesosphere. Var(T') values become particularly large as waves

propagate upwards and the wave amplitudes increase in response to the decrease of air density with height. Large values of Var(T') result in unrealistically high values for K_{Dyn} (via Equation 11) which are then used to diffuse atmospheric constituents and temperature, leading to the generation of numerical instabilities.

It is expected that this discrepancy arises because the WACCM parametrization does not consider the wave- and turbulence-induced diffusive damping of the wave amplitude. Damping of wave amplitudes by the viscosity of the atmosphere can limit wave amplitude growth with increasing altitude. This effect was first examined by Hines (1960) and then extended by Pitteway and Hines (1963) to include both viscous and conductive dissipation. The theory was further extended by Weinstock (1976); Weinstock (1982, 1984a, 1984b, 1990) to include wave-induced damping. Weinstock argued that the amplitudes of waves of all scales are limited by the diffusion-like processes related to the motions of the smaller-scale waves and turbulence.

By ignoring radiative cooling, which is small in the atmosphere below the thermosphere, and combining Weinstock's results with those of Pitteway and Hines (1963), we modified the wave stress profiles produced by the WACCM gravity wave drag parametrization introducing the following amplitude growth factor (see Appendix B for details on the formulation of the wave damping):

$$\tau(z_0 + n\Delta z) = \tau_{WACCM}(z_0 + n\Delta z)\exp\left[-2\sum_{l=0}^{n-1}\lambda_{wave}(z_0 + l\Delta z)\Delta z\right] \tag{16}$$

$$\lambda_{wave}(z) = \frac{N^3}{k(\overline{u} - c)^4}(K_{wave} + K_{zz}) \tag{17}$$

where τ is the damped wave stress profile, τ_{WACCM} is the original (undamped) wave stress profile provided by WACCM, k is the horizontal wave-number, $\overline{u}$ is the background wind, Δz is the vertical grid-spacing, and $n = [1, N]$ and $l = [0, n-1]$ indicate the model level number. n is the lowest model level where damping is applied, and N is the last model level (i.e., the model top). Note that, for simplicity, in the formulation above Δz is assumed to be constant; in the model, vertical levels are not equally spaced and Δz is calculated accordingly.

τ is calculated iteratively starting at the tropopause altitude ($z_0 \sim 12$ km), where $K_{wave} + K_{zz}$ is negligible, and proceeding upward. At z_0, $\tau = \tau_{WACCM}$ and Var(T'), the associated K_{wave} and λ_{wave} are computed via Equations 13–15, 10 and 17. At the lowest altitude where the damping is applied ($n = 1$), $\tau(z_0 + \Delta z)$ is computed using K_{wave} and K_{zz} from the level below (i.e., z_0) according to (16). The damped wave stress τ is then used to compute Var(T')$(z_0 + \Delta z)$ and $K_{wave}(z_0 + \Delta z)$ using Equation 13-15 and 10.

The process is repeated to derive Var(T') and K_{wave} profiles into the lower thermosphere that now include diffusive damping by waves and turbulence. The Var(T') profiles computed in this way compare favorably with observations (not shown). Note that, according to Equations 16 and 17 the effectiveness of the wave damping varies depending on the value of $(\overline{u} - c)$. Therefore, not all waves are damped in the same way since the amplitude growth factor depends on the background wind variations with height and on the wave phase speed. In the MLT region, at those heights where the background wind $\overline{u}$ approaches zero as it reverses, the wave diffusive damping is most effective for low-frequency, long-period gravity waves and is thus generally more efficient for that portion of the spectrum characterized by smaller c.

Figure 1 shows an example of how the wave damping works for instantaneous values at a single grid-point. The number of vertically propagating waves available at each height for the computation of Var(T') via Equations 13–15 is shown in panel a. Out of the 64 waves excited at the wave source in the troposphere, at 50 km about 50 waves are still propagating upward. This number decreases with height as waves dissipate and are removed from the spectrum. At ~120 km all waves have been dissipated. In panel b, the variation of the background wind with altitude is shown. The winter westerlies become easterlies at ~80 km. The undamped and damped momentum flux profiles across the wave spectrum are shown in panels c and d, respectively. The effectiveness of the wave damping (defined as the ratio between the damped and undamped momentum fluxes) is shown in panel e. Finally, panel f shows the temperature perturbations derived using the damped momentum fluxes of panel d via Equations 13–15.

At 80 km, where $\overline{u} \sim 0$ (Figure 1b), the 45 vertically propagating waves (Figure 1a) that carry momentum flux have phase speeds from $c = -50$ to $c = +60$ m s^{-1} (Figure 1c). When the wave damping is applied to these waves

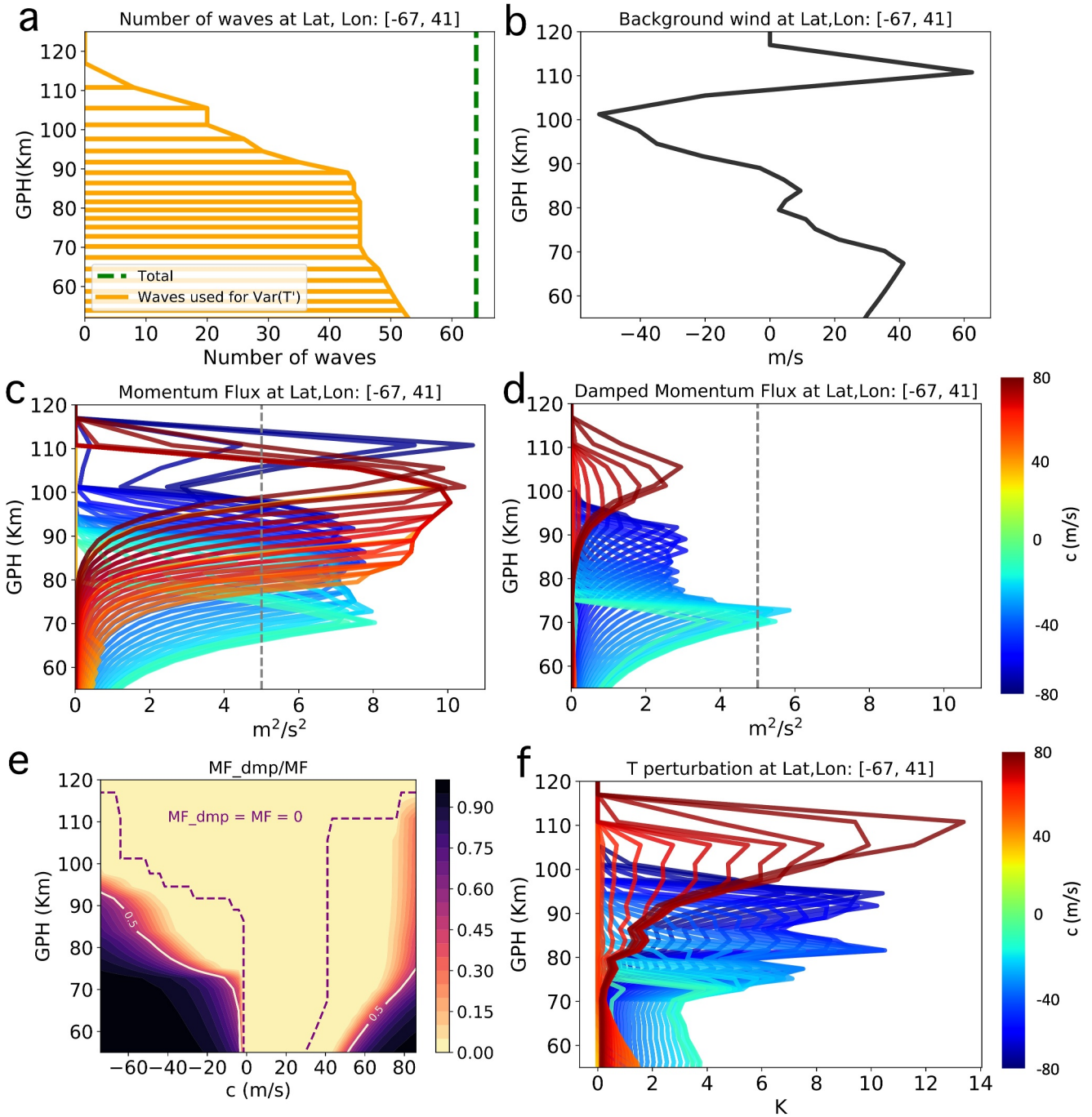

Figure 1. Demonstration of how the wave diffusive damping works for a single grid-point at 67°S, 41°E. All variables shown are instantaneous values for the same time step. Panel (a) shows the total number of waves excited at the surface (i.e., within the troposphere) (green line), and the number of waves that are still propagating upwards above 50 km (orange line) and that are used for the computation of Var(T'). Panel (b) is the background wind. Panel (c) shows vertical profiles of the WACCM parametrized momentum fluxes across the wave spectrum. Panel (d) shows the same momentum fluxes after the wave diffusive damping is used (Equation 16). In panel (e), the ratio between the damped and undamped momentum fluxes in panels (d) and (c) is shown as a function of wave phase speed and height. The solid contour line indicates where the ratio MF_{dmp}/MF halves. The dashed contour line indicates regions where $MF_{dmp} = MF = 0$ (i.e., there are no waves to be damped). Panel (f) shows the amplitude of the gravity wave-induced temperature perturbations computed using the damped momentum fluxes of panel (d).

(Figure 1d), all positive phase speed waves (red lines) are significantly damped; in contrast, fast-traveling gravity waves with large and negative phase speeds (blue lines) are less significantly affected. For these waves the damping is about 50% effective, since the momentum flux they carry has been almost halved. The solid 0.5

contour line in Figure 1e shows the threshold c value for which the wave damping becomes less than 50% effective. At 80 km waves with phase speed less than -40 m s^{-1} (moving toward left in the graph) are damped by less than 50%, all other waves with negative and positive phase speeds (moving toward the right in the graph) are damped by 50% or more of their original amplitude. As explained above, the effectiveness of the wave damping depends on the variation of the background wind with height. At this particular grid-point, the wave damping is the least effective at 70 km where almost all waves with a negative phase speed are damped by less than 50% (see also Figures 1c and 1d, blue lines).

To conclude this section, it is important to stress that the damped wave stress profiles of Equation 16 are only used for the computations of Var(T'), and thus for K_{wave} and K_{Dyn}, but not for the computation of the wave drag. This means that the WACCM gravity wave drag formulation has not been modified in any way, and the model uses the original (undamped) Reynolds stress profiles for evaluating the saturation condition and dissipating waves. The need for introducing the wave diffusive damping to get reasonable estimates for T' indicates that the gravity wave drag currently computed by the model (using the undamped wave amplitudes) might be too large in the MLT. Likely, tuning the wave source spectrum overcame this issue, but a more consistent treatment of gravity waves in the future will require a revision of the current drag computation by using the damped stress profiles and refining the tuning of the spectrum accordingly.

2.2.2. Maximum Value for K_{Dyn}

On a few occasions, we found that not all gravity waves within the spectrum are dissipated throughout the model's vertical column (see Figure S1c in Supporting Information S1). In the current version of the model, the stress carried by these waves that never dissipate is artificially set to zero when they reach the model top. This approach works for the computation of the gravity wave drag because the wave stress is only used to evaluate the drag when waves dissipate and is ignored otherwise. However, when waves propagate to the model top, their amplitude become extremely large (Figure S1d in Supporting Information S1), and so does the associated Var(T'). This leads to the computation of very large K_{wave} and K_{Dyn} (Figure S1b in Supporting Information S1) that will eventually cause the model to become unstable when diffusion is applied.

To keep the model stable, we defined an upper limit for the maximum value of K_{Dyn} so that it cannot become larger than the maximum value of the eddy diffusivity within the vertical column, K_{zz_MAX} (see Figure S1 in Supporting Information S1 for an example of how this is done). K_{Dyn} was found to be 5 times larger (or more) than K_{zz_MAX} near the model top (Figure S1a in Supporting Information S1). This very large value of K_{Dyn} was promoted by fast-traveling, large amplitude, gravity waves (Figure S1d in Supporting Information S1). Note that these are also the waves for which the wave damping presented above is less effective.

This approach was found to be the most suitable, physically-based approach to bound K_{Dyn}, based on the fact that K_{zz} is itself bounded within the model code to prevent non-physical values. K_{zz} is a function of the gravity wave-induced wind tendencies (u'_{gw}). After the evaluation of the wave stress divergence, and thus the computations of u'_{gw}, the maximum values of u'_{gw} are bounded so that very large wind tendencies that would cause numerical instabilities cannot be simulated. The need to bound excessively large wave fluctuations is already present within the WACCM gravity wave drag scheme and we used the same approach to bound our new diffusivity.

3. Methods

3.1. Numerical Simulations

In this work, CESM2-WACCM6 simulations were run for the historical period from the year 2000 to 2012. WACCM6 is a state-of-the-art chemistry climate model able to realistically simulate the chemistry and dynamics of the stratosphere and middle atmosphere (Gettelman et al., 2019). Our simulations are atmosphere-only simulations that use CMIP6 atmospheric emissions and specified historical SSTs and sea ice extent. We employed the FWmaHIST model configuration that uses a ∼2° horizontal nominal resolution (1.9° in latitude and 2.5° in longitude), 70 vertical levels with variable grid-spacing from ∼1 km in the troposphere to ∼3.5 km above 65 km, and a finite volume dynamical core. For the representation of atmospheric chemistry, we used the WACCM middle atmosphere (MA) chemistry package with a reduced set of tropospheric reactions.

In all our simulations, the meteoric sodium and iron chemistry models first presented in Feng et al. (2013) and Marsh et al. (2013) are used and added to the standard WACCM chemistry model. We use here the latest version of the Fe and Na models as in Daly et al. (2020) and Jiao et al. (2022). Na and Fe are injected into the MLT by employing a Meteoric Input Function that specifies the input of Na and Fe as a function of season and latitude (see also Section 3.1.1).

For our control simulation (from now on termed the "CTRL" run), WACCM6 is run using the default gravity wave drag parametrization. When the model is run with the new gravity wave transport parametrization, we refer to it as "K_DYN." The frequency of all model outputs are monthly averages.

3.1.1. Meteoric Input Function

The Meteoric Input Functions (MIFs) for Na and Fe were estimated by combining the new version of the Chemical ABLation MODel version 3 (CABMOD-3) (Carrillo-Sánchez et al., 2016, 2020) with the Zodiacal Cloud Model (ZoDY) (Nesvorný et al., 2011). CABMOD-3 simulates the ablation of the major meteoric elements from an individual dust particle, which is set to have a 90 wt% Fe-Mg-SiO_4 phase and a 10 wt% metallic Fe-Ni phase (with an elemental Fe:Ni ratio set to 5.5), so that about 70% of the total Fe is embedded inside the silicate bulk (Bones et al., 2019; Carrillo-Sánchez et al., 2020). ZoDY provides the mass, velocity and radiant distributions of dust particles entering Earth's atmosphere from Jupiter Family Comets, the asteroid belt, and long-period (Halley-Type and Oort Cloud) comets, and the relative contributions from these different sources are weighted using the procedure described by Carrillo-Sánchez et al. (2016). The MIF then describes the vertical injection profile of each metal, and these are set to vary with season and latitude as described in Feng et al. (2013): an autumnal maximum and a vernal minimum, with the amplitude increasing from essentially no variation at the equator to ±30% at the poles.

In the standard version of WACCM (Daly et al., 2020; Jiao et al., 2022), both the Na and Fe MIFs have to be reduced by a factor of 5 from the CABMOD-ZoDY profiles (Carrillo-Sánchez et al., 2020), in order to achieve satisfactory agreement with lidar observations of Na and Fe. This factor accounts for WACCM underestimating the vertical transport of minor species through the MLT because small-scale gravity waves are not resolved, as we will see next. For the current work, the CABMOD-ZoDY profiles were reduced by a factor of 2 for both the CTRL and K_DYN simulations. The resulting Na and Fe MIFs are shown in Figure S2 in Supporting Information S1. See Section 4.2 for further discussion on the implications of using larger MIFs in this study.

3.1.2. Analysis of Results

For the analysis of the results we used the period 2008–2011. All variables shown in the study are climatologies computed over this period, unless otherwise specified. This period was selected based on the availability of the observational products used for model-observation comparisons (see also Section 3.2).

For model-observation comparisons presented as a function of altitudes (km), this is the geometric altitude. For the observational data sets, the geometric altitude is available directly from the observations. For model outputs, the model's geopotential height (gph) is converted into geometric altitude (h) according to $h = (r \cdot gph)/(r - gph)$, where r is the Earth's radius.

The annual and semi-annual oscillations presented in Section 4.2.1 were analyzed in the following way: (a) the monthly anomalies of the Na and Fe total column abundances against the annual mean were first computed at each latitude for both CTRL and K_DYN; (b) the anomaly signal was decomposed into its annual and semi-annual components by fitting the following harmonic function (H) onto the anomaly time-series at each latitude:

$$H = a_1 \cos\left[\frac{2\pi}{365}(t - b_1)\right] + a_2 \cos\left[\frac{4\pi}{365}(t - b_2)\right] \quad (18)$$

where t is the time (in days), a_1 is the amplitude of the annual oscillation, a_2 is the amplitude of the semi-annual oscillation, b_1 is the phase of the annual oscillation, and b_2 is the phase of the semi-annual oscillation. The coefficients a_1 and b_1 of the harmonic fit are used in the discussion of the results to explore differences between CTRL and K_DYN.

Finally, note that for the analysis of the gravity wave-induced wind tendencies in Figure 8, only large phase speed ($|c| > 40$ m s^{-1}) gravity waves generated by fronts are shown and discussed. This was done for figure clarity, since tendencies from waves generated by convection and from medium- and low-speed gravity waves were (for that particular location) one order of magnitude smaller and their contribution to the total was secondary.

3.2. Observational Data Sets

3.2.1. Fe and Na Lidar Observations

We use here published Fe and Na ground-based lidar and satellite observations (Feng et al., 2013; Gardner et al., 2005; Marsh et al., 2013; States & Gardner, 1999) for which we provide a short description.

Lidar observations come from three stations located at middle and high latitudes: Urbana (40°N, 88°W), Rothera (68°S, 68°W) and South Pole (90°S). The data was collected during observational campaigns carried out in different decades between the late 1990s and the early 2000s: Fe measurements were made at Urbana between 1995 and 1996, at the Rothera research station between 2003 and 2005, and at South Pole between 1999 and 2001. Na measurements were carried out at Urbana between 1996 and 1998, and at South Pole between 1995 and 1997.

For lidar measurements, the instrument calibration error is in the order of ±10%. In addition to this, uncertainty in the measured metal densities comes from geophysical noise (due to fluctuations induced by planetary waves, tides, and gravity waves), which has been quantified for the three stations considered here and is reported in Table S1 in Supporting Information S1.

Global coverage for the Na total column abundance is derived from the Optical Spectrograph and Infra-Red Imager System (OSIRIS) spectrometer on the Odin satellite for years 2003 and 2009 (B. Yu et al., 2022). Measurement gaps were filled in with lidar observations from the late 1990s (see Marsh et al., 2013, for details). The global field was constructed using zonal monthly averages of the absolute Na density discretized in 10° latitude bins. A typical uncertainty for OSIRIS retrievals near the sodium layer peak is ∼10%; however, for some latitudes, the uncertainty can be up to ±30% depending on the number of profiles available in each latitude bin (Fan et al., 2007).

As explained above, our model-observation comparisons are carried out for the period 2008–2011. Although the Fe and Na observations derive from different decades, the comparison is acceptable since the Fe and Na layer do not seem to be significantly affected by climate change (see e.g. Dawkins et al., 2016).

3.2.2. MIPAS Temperature and CO_2 Data

The most recent MIPAS (Michelson Interferometer for Passive Atmospheric Sounding) CO_2 and temperature observations were used to assess model performance. We used the MIPAS CO_2 data version V8_CO2_661. This corresponds to an upgrade of V5_CO2_622, which was described by Jurado-Navarro et al. (2016) and validated in López-Puertas et al. (2017), and a short description of what is new in V8 is given below. CO_2 is retrieved from the Upper Atmosphere (UA) mode of MIPAS spectra. The new version includes several updates to the level-2 algorithm that aim at addressing issues encountered in validation activities and science studies. First, in the retrieval we used the most recent version of the level-1b spectra, version 8.03, recently distributed by the European Space Agency (ESA). These new level-1b data improved on previous versions in several ways, particularly by the use of a time-dependent model of detector non-linearity (see Kiefer et al., 2021, for more details). Also, in this CO_2 data set we used an improved new version of the MIPAS kinetic temperature (García-Comas et al., 2023). This is retrieved from the 15 μm spectral region up to an altitude of approximately 115 km (García-Comas et al., 2023), which is merged with the temperature above that altitude obtained from the joint retrieval of temperature and NO concentration from the 5.3 μm region (Funke et al., 2023). While improvements in both regions (below and above 115 km) are documented in the works mentioned above, since the kinematic temperature has a significant effect on the retrieved CO_2, we provide in Supporting Information S1 of the present study a brief summary of the temperature retrieved from the CO_2 15 μm (see Text S2 in Supporting Information S1 for details).

The main difference between V8 and V5 for CO_2 is that in V8 we have smaller (∼5%–10%) CO_2 mixing ratios between 90 and 130 km. In more detail, for the time series at 60°S–60°N shown in Figure 14 of López-Puertas et al. (2017), the new data set shows: (a) marginal effects (slightly larger CO_2) at 90 km; (b) significantly smaller CO_2 vmr at 100 km (∼15 ppmv) and 110 km (∼10 ppmv); (c) very similar values at 120 km; and (d) slightly

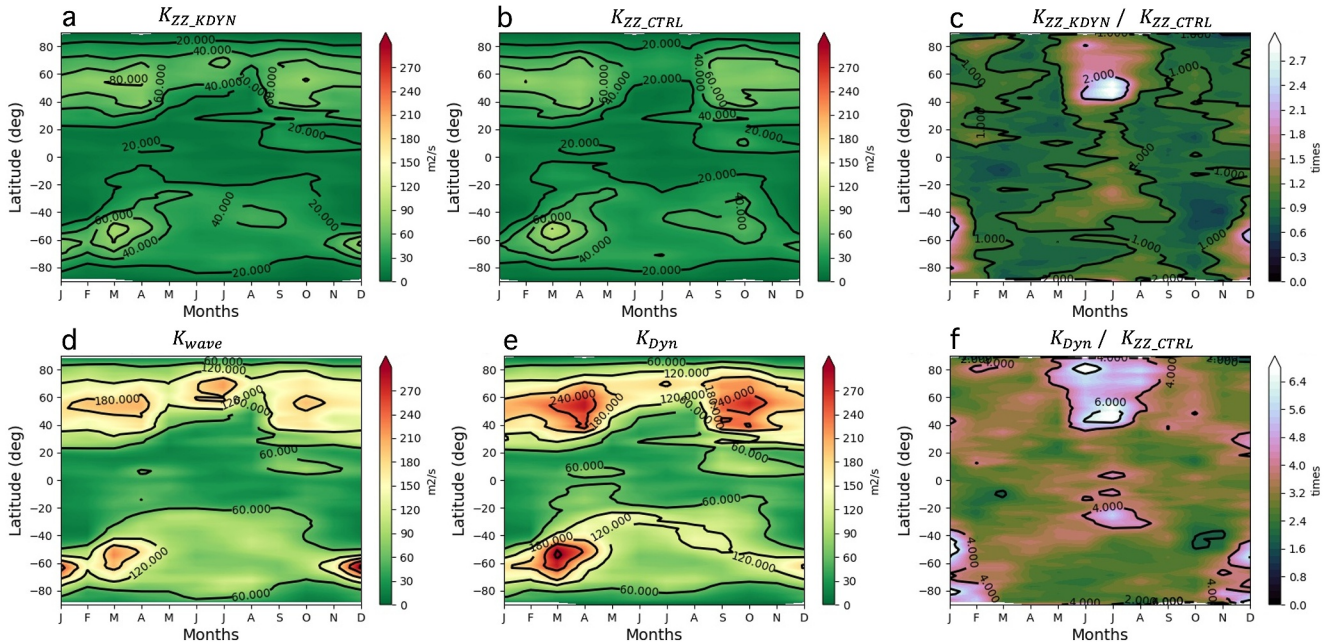

Figure 2. Seasonal variation of (a) K_{zz} for K_DYN (K_{zz_KDYN}), (b) K_{zz} for CTRL (K_{zz_CTRL}), and (c) their ratio. Seasonal variation of (d) K_{wave}, and (e) K_{Dyn} for K_DYN. Panel (f) is the ratio between K_{zz_KDYN} and K_{zz_CTRL}. All panels show model outputs at $p = 0.005$ hPa ~82 km (~mesopause).

smaller values, ~3–4 ppmv, at 130 km. An analogous comparison for the polar regions, 65°N–85°N and 65°S–85°S, shows that the changes are similar but also show smaller values (~5 ppmv) at 120 km. As a note, we should mention that in the new version the data have been filtered to have smaller residuals ($\chi^2 \leq 2.3$). As for the errors in this data set, we do not expect them to change significantly from the previous version (Jurado-Navarro et al., 2016).

For temperature, we used here the MIPAS temperature data version V8_T_661 retrieved from the CO_2 15 μm emission in the Upper Atmosphere (UA) mode (García-Comas et al., 2023). This is an upgrade version of the previous one, V5_T_611, which has been described in detail in Garcia-Comas et al. (2014). The new version has been improved in several aspects. Among others, the most recent version of L1b spectra, the a priori temperature, and a new atomic oxygen concentrations required for the non-LTE calculations. A detailed description of the new data version is given in García-Comas et al. (2023).

The noise error for individual profiles of the MIPAS temperature data version V8_T_661 is smaller than 1 K at altitudes below 60 km, 1–3 K at 60–70 km, 3–5 K at 70–90 km, 6–8 K at 90–100 km, 8–12 K at 100–105 km and 12–20 K at 105–115 km. These errors do not exhibit a significant dependence on latitude or season, although they slightly increase around the polar summer mesopause (Garcia-Comas et al., 2014). The systematic errors are generally smaller than 0.7 K below 55 km, 1 K at 60–80 km, 1–2 K at 80–90 km, 3 K at 95 km, 6–8 K at 100 km, 10–20 K at 105 km, and 20–30 K at 115 km Garcia-Comas et al. (2014).

Here we use MIPAS data for the period 2008–2011 for both CO_2 and temperature. Data was filtered for quality following López-Puertas et al. (2017). All satellite data was re-gridded onto a 1° regular latitude-longitude grid. For multiple data-points falling into a same 1 × 1° grid-box the mean value within the box is calculated and used.

4. Results and Discussion

4.1. K_{dyn} and K_{zz}

In this section, we analyze how the model total diffusivity changes when K_{zz}, in CTRL, is replaced by the new dynamical diffusivity K_{Dyn} in the K_DYN run. From Figures 2b and 2e, we can see that the seasonality of the model diffusivity between CTRL and K_DYN is unchanged. K_{Dyn} (Figure 2e) is however much larger than K_{zz} (Figure 2b) everywhere, so that in the K_DYN run, atmospheric constituents (and temperature) are mixed more

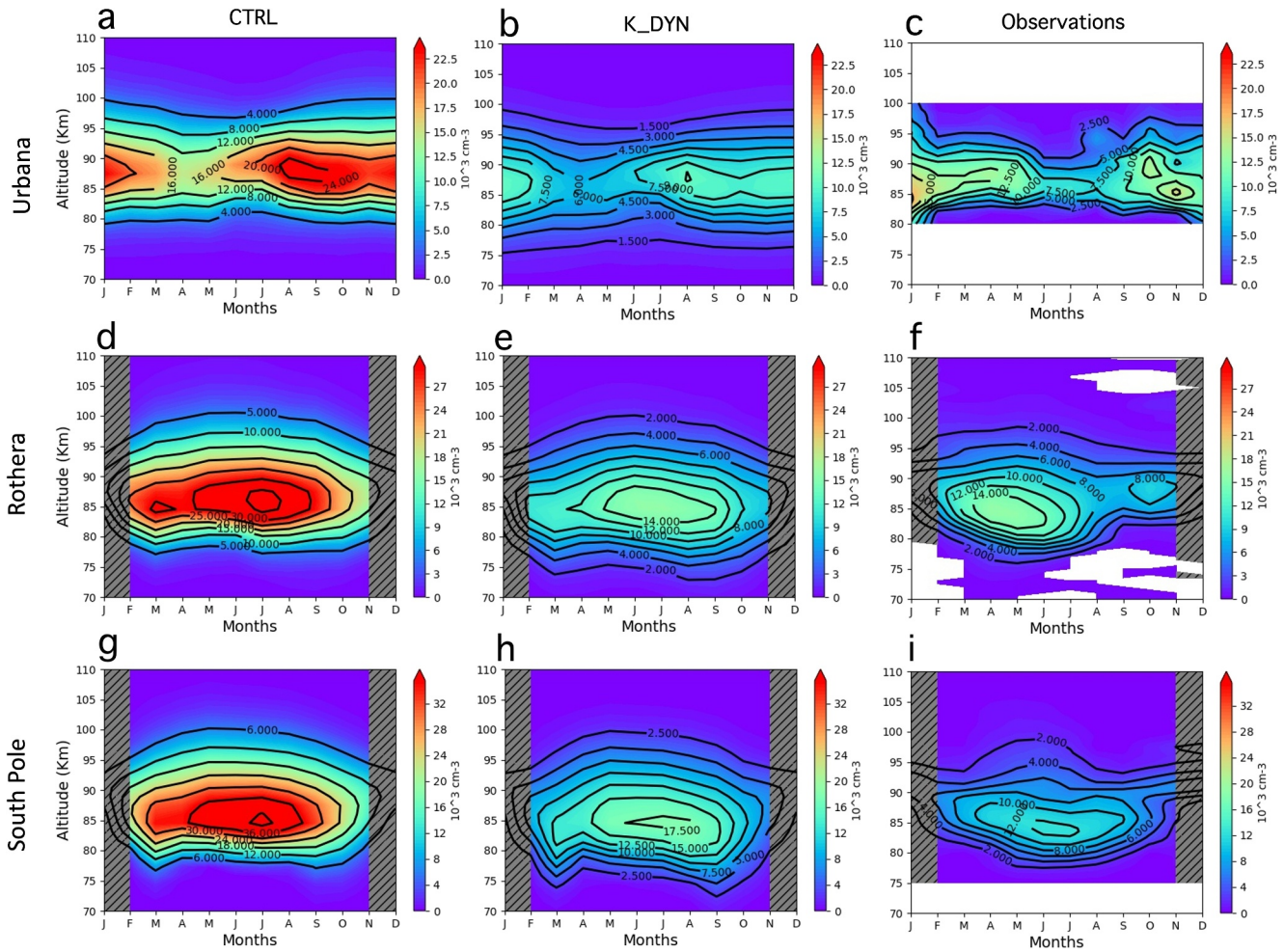

Figure 3. Model-observation comparisons for Fe concentration at Urbana (a, b, c), Rothera (d, e, f) and South Pole (g, h, i). For Rothera and South Pole, PMC months are hatched since removal of Fe on the ice surface is not included in this version of WACCM.

vigorously than CTRL. This is expected, since according to Equation 4, K_{Dyn} includes contributions from breaking (K_{zz_KDYN}, shown in Figure 2a) and non-breaking (K_{wave}, shown in Figure 2d) gravity waves.

While the overall seasonality of the gravity wave mixing is conserved in K_DYN, with two distinct maxima in spring and autumn at ~82 km, the total diffusivity does not increase in the same way across different latitudes. By examining the ratio between K_{Dyn} and K_{zz_CTRL} (Figure 2f) we can see that K_{Dyn} is 4–6 times larger than K_{zz_CTRL} at mid- to high latitudes (above/below 40°N/S) during the summer months, and at southern tropical latitudes (~30°S) during the winter months (JJA) (also note that a similar but weaker signal is detectable at ~30°N during DJF). Hence the impact of a larger diffusivity is not homogeneous across seasons and/or geographical areas.

The K_{Dyn}/K_{zz_CTRL} ratio maximizes where the K_{zz_KDYN}/K_{zz_CTRL} ratio is also the largest (Figure 2c), indicating that it is K_{zz} changes to drive the heterogeneous increase in total diffusivity. K_{zz} in K_DYN is twice as large as K_{zz_CTRL} at ~40°N (Figure 2c), this is also where $K_{Dyn}/K_{zz\_CTRL} \sim 6$ (Figure 2f).

In K_DYN, K_{zz} increases because of changes in the gravity wave forcing. In particular, gravity waves break at different altitudes than in CTRL and generate a larger degree of mixing. Changes in altitude and strength of the gravity wave breaking are driven by a decrease/increase of the atmospheric stability near the mesopause between CTRL and K_DYN, as described in detail in Section 4.3.

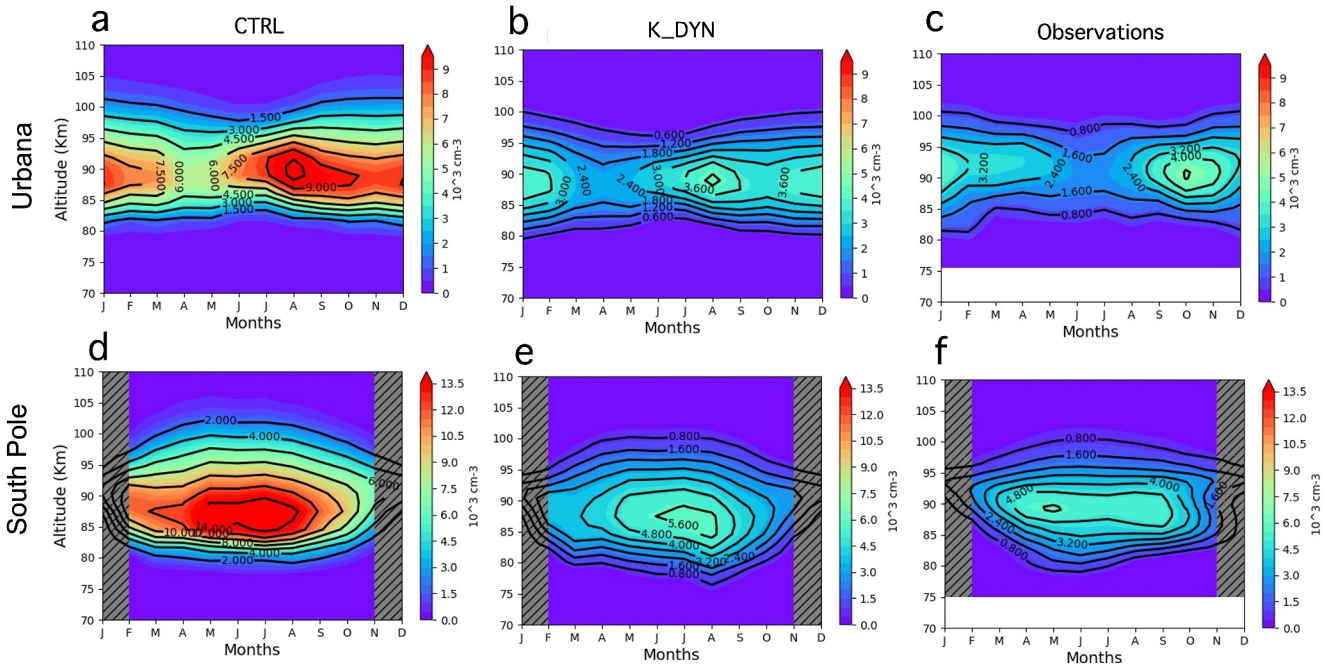

Figure 4. Model-observation comparisons for Na concentration at Urbana (a, b, c), and South Pole (d, e, f). For South Pole, PMC months are hatched since removal of Na on the ice surface is not included in this version of WACCM.

4.2. Modeling the Metal Layers: Na and Fe Densities

We discuss next the impact of wave-induced constituent transport on mesospheric iron and sodium. Figures 3 and 4 show model-observation comparisons for Fe and Na at selected sites where lidar observations are available. Note that, for the high-latitude sites, months corresponding to the polar mesospheric cloud (PMC) seasons are hatched since comparisons with model data are not reliable for these months due to the removal of metallic species on the ice cloud surfaces (Plane et al., 2004), which are not modeled in this version of WACCM. In Figure 5, the global field of the Na total column abundance is shown for CTRL, K_DYN and observations.

The CTRL simulation, even if the MIF was decreased by a factor of 2, largely overestimates metal densities at all sites, confirming that the vertical transport of these species is too weak in the current WACCM model. In K_DYN, the larger vertical mixing associated with non-breaking gravity waves causes the downward fluxes of atmospheric Fe and Na to increase, dramatically improving the model-observations agreement at the lidar locations (mid- and high latitudes) (Figures 3 and 4), and also globally (Figure 5). When the Na and Fe atoms are transported downwards they are removed by forming stable reservoir species (e.g., NaHCO3 and FeOH) which then polymerize into meteoric smoke particles below 85 km (Plane et al., 2015). Thus, the net effect of the new

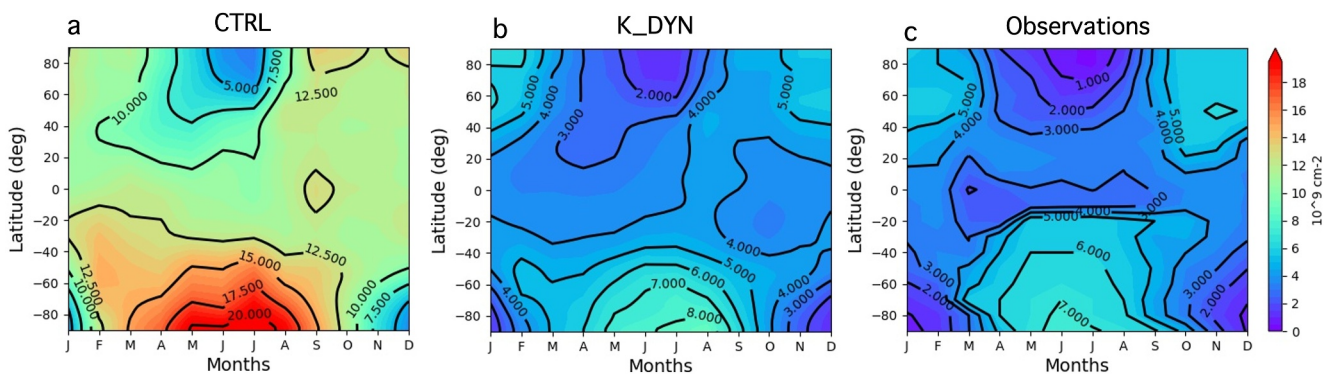

Figure 5. Na total column abundance as a function of latitude and month for CTRL (a), K_DYN (b) and observations (c).

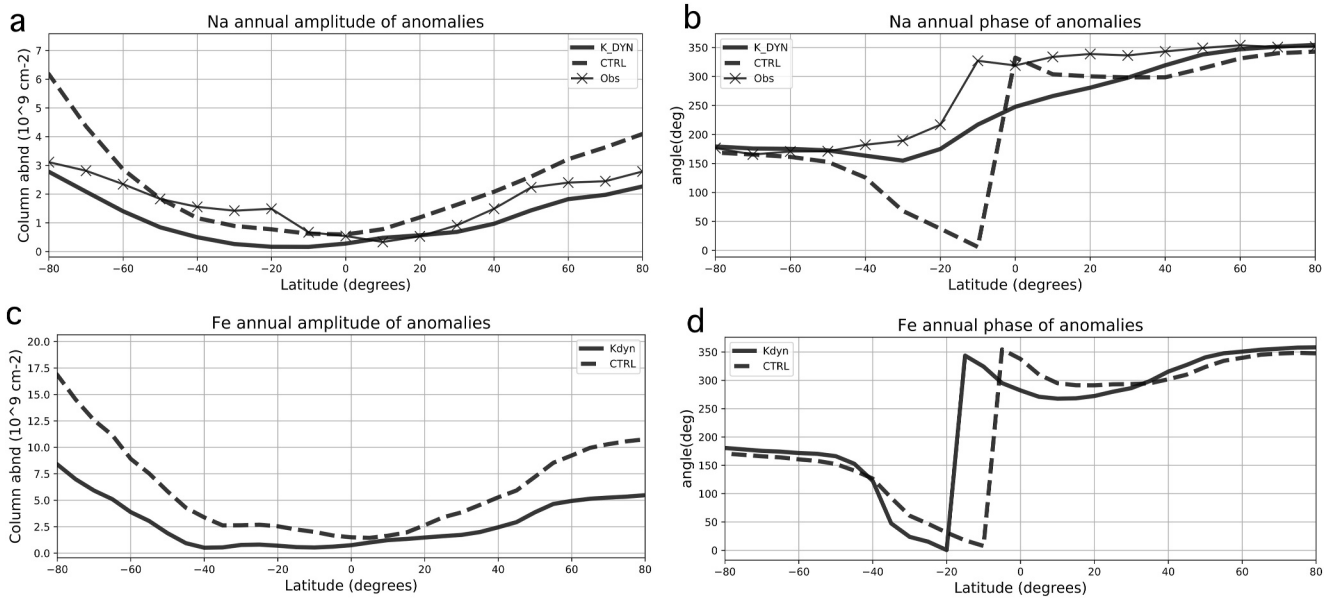

Figure 6. Amplitude (a, c) and phase (b, d) of the annual oscillation of the Na and Fe total column abundance anomalies (against annual mean) as a function of latitude for K_DYN (solid line) and CTRL (dashed line). For Na, the AO amplitude and phase derived from observations (crosses) are also shown.

total dynamical diffusivity K_{Dyn} is not only to change the metal layer vertical structure, but also to reduce the overall metal atom densities and the total column abundance, as shown in Figure 5.

We note that, at Urbana, K_DYN tends to underestimate Fe and Na concentrations compared to observations, although the modeled Na concentration generally falls within two standard deviations of the observational mean (see Figure S3 in Supporting Information S1).

At high southern latitudes, that is, at South Pole (Figures 3g–3i, Figures 4d–4f) and between 60 and 80°S (Figure 5), K_DYN overestimates the observational mean, especially in winter. Previous studies (Feng et al., 2013; Gardner et al., 2011; Gardner & Huang, 2016) have linked the WACCM high winter concentrations of sodium and iron at high southern latitudes to two processes: the strength of the meridional circulation, via mass convergence toward the poles in winter; and the positive temperature dependence of the reactions by which the reservoir species FeOH is converted into Fe.

As for the temperature, at high southern latitudes, K_DYN winter mesospheric temperatures agree well with observations at $\sim 10^{-3}$ hPa and just above (see Figures S15 and S17 in Supporting Information S1). This is approximately where the metal layer has its centroid (between 87 and 91 km for Rothera and South Pole, see Table S1 in Supporting Information S1) and where the Fe and Na concentrations are overestimated to a greater extent. It is therefore unlikely that a misrepresentation of temperature is responsible for the metal density overestimation.

As we shall see later in Section 4.3, K_DYN induces a stronger residual meridional circulation than CTRL. We do not have clear indications of whether the meridional circulation is too strong in our model compared to the real world. Therefore, we cannot rule out that a too-large horizontal transport of Fe and Na toward the winter poles might be responsible, at least in part, for the overestimation of the metal concentration at those latitudes.

Another possible reason for the winter overestimation of the metal atom densities at high southern latitudes is that the removal of metals by downward transport might still not be large enough at these latitudes. K_{dyn} might be too weak over the southern hemisphere polar cap because of the underlying representation of gravity waves within the WACCM model. Modeling gravity waves over the Antarctic continent is notoriously challenging. The lack of gravity wave drag (particularly, it is thought, of the orographic type) has been suggested to account for a major model bias in reproducing Southern Hemisphere polar winds and temperature across multiple climate models (e.g., Cámara et al., 2016; Garcia et al., 2017; McLandress et al., 2012). In WACCM6, modifications to the orographic gravity wave drag source function were introduced and greatly improved model-observations

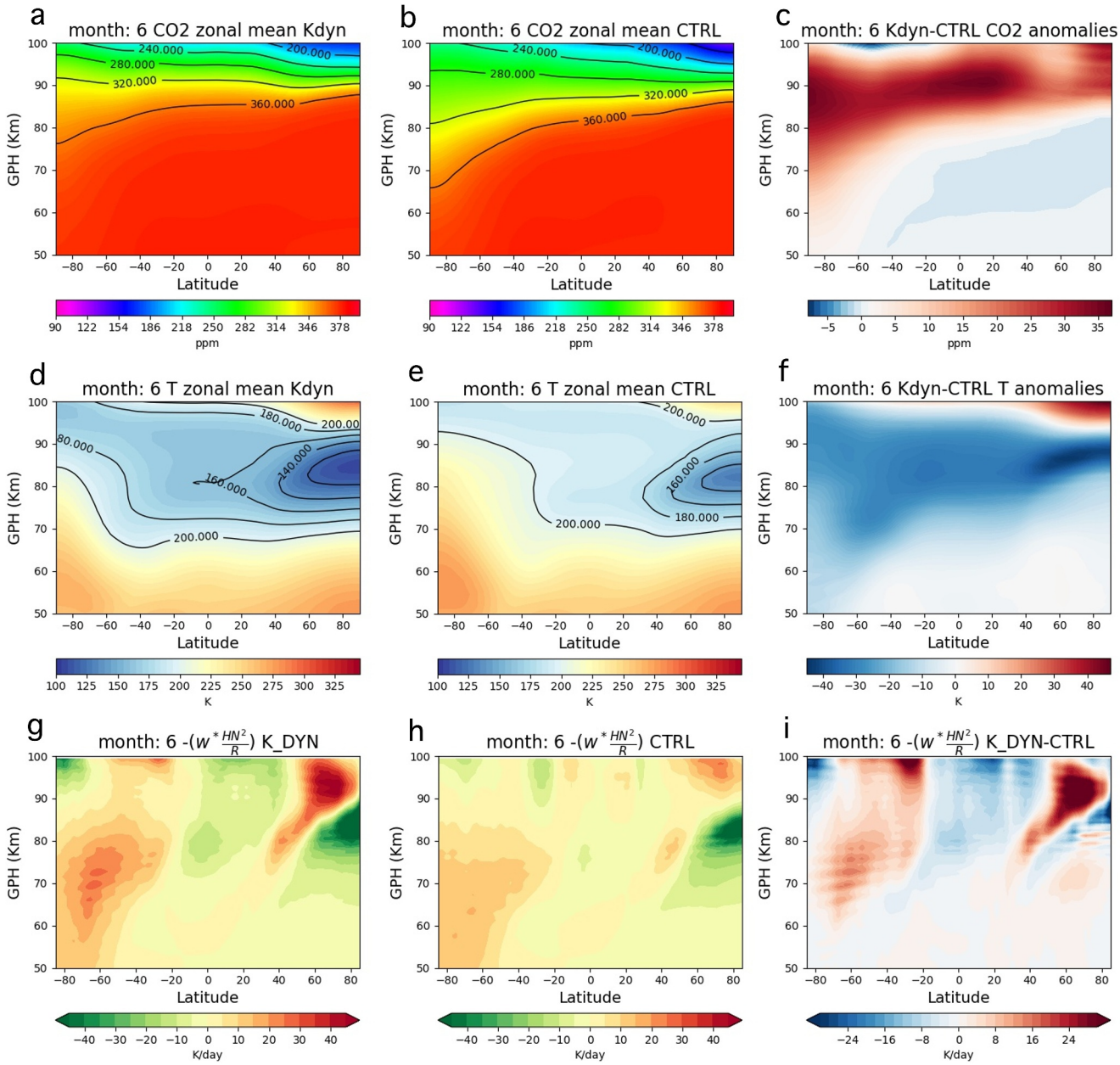

Figure 7. Zonal mean cross-sections of CO_2 mixing ratio, air temperature (T), and expected temperature departure from radiative equilibrium $\left(-w^*\left(\frac{HN^2}{R}\right)\right)$ as simulated by K_DYN (a, d, g), CTRL (b, e, h) and their difference (c, f, i) for Northern Hemisphere summer conditions (June).

agreement following the work by Garcia et al. (2017). In the same study, however, the authors point out that the circulation of the upper atmosphere in high-top models is highly sensitive to the tuning of the gravity wave drag (of any type) over the Antarctic continent, and that our knowledge of the distribution of the gravity wave stress across different sources is still limited. Additionally, Liu (2019) showed that at high southern latitudes the parametrized gravity wave forcing in the stratosphere and lower mesosphere is too weak in WACCM, giving rise to a too strong winter westerly jet compared to climatologies. K_{dyn} computations rely on the spectrum of waves specified at the surface by the WACCM gravity wave drag parametrization (see Section 2.2), so if the gravity wave drag is not represented properly, especially in regard to the height at which waves break, the counterpart of propagating gravity waves will also be affected.

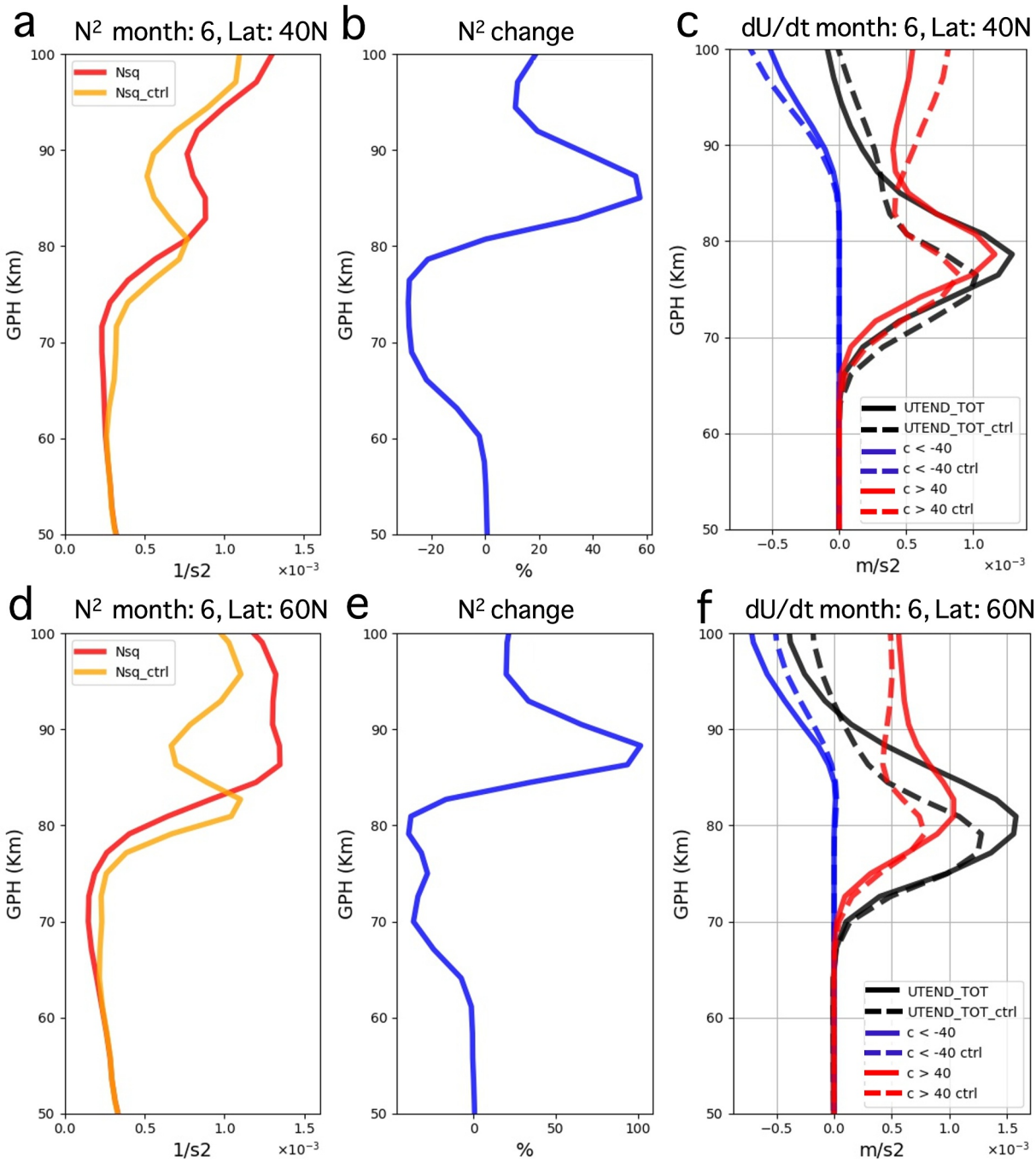

Figure 8. Vertical profiles of the squared Brunt-Väisälä frequency (N^2) for K_DYN (red line) and CTRL (orange line) (a, d), and its percentage change relative to CTRL (b, e). Total wind tendencies generated by gravity wave breaking (black line), and fraction of total tendencies associated with fast eastward (red line) and westward (blue line) traveling gravity waves (c, f) for K_DYN (solid line) and CTRL (dashed line). All profiles are for Northern Hemisphere summer conditions (June) and averaged over 40°N (a, b, c) and 60°N (d, e, f).

From Figure 5 we can see that K_DYN underestimates somewhat (1–2 × 10^9 atom cm^{-2} ~ 15%–30%) the observed Na total column abundance at mid- to low southern latitudes (~20°S–40°S) in winter. This is an inherited bias from the sodium layer model employed by WACCM. In the observations, large values of the total column abundance extend from high to low southern latitudes from April to September. This behavior is not replicated by either CTRL or K_DYN, where large column abundance values remain confined to high latitudes (greater than 40 S). It is worth pointing out, however, that particularity in this region the observational uncertainty

is large due to the lack of measurements for the winter hemisphere from April to August between 20 and 80°S (Fan et al., 2007; Marsh et al., 2013). The global Na field was computed via interpolation using the available data for the southern hemisphere spring and summer months (September to March) (see Marsh et al., 2013, for details), so model-observation comparisons in this region must be treated with caution.

Note that, as described in Section 3.1.1, K_DYN employs Na and Fe MIFs that are within a factor of 2 of the most recent estimates (Carrillo-Sánchez et al., 2020; Hervig et al., 2021). This is a significant improvement in the model's skill compared to the standard WACCM configuration, where the MIFs had to be reduced by a factor of 5 (i.e., we use here MIFs that are 2.5 times larger). While a factor of 2 falls within the uncertainty of the MIFs estimates, we note that the model still needs to use a smaller MIFs than predicted to compare favorably with observations. This might be due, at least in part, to the theoretical assumptions made in Section 2.1 for which we neglect the compressibility of the wave fluctuations and the Stokes drift induced by the spectrum of propagating waves. When these assumptions are removed, theory predicts that all sources of vertical transport (i.e., molecular diffusion, eddy mixing, and wave mixing) are enhanced in the mesopause region (Gardner, 2024). In addition, K_DYN does not include the chemical flux for either Na or Fe that arises when the unresolved, parametrized waves modulate the chemical reactions involving these species, thereby increasing their chemical losses on the layer bottom sides (Gardner & Liu, 2016). A larger vertical transport and the inclusion of the unresolved Na and Fe chemical fluxes might allow the use of a larger MIF, thus brining the model's MIFs closer to their true values.

To conclude this section, we stress that the much improved representation of the metal layers in K_DYN endorses modeling and observational-based studies suggesting that the mixing by vertically propagating non-breaking gravity waves must be taken into account to properly represent the global distribution and magnitude of species like Na and Fe in the upper layers of the atmosphere.

4.2.1. Annual and Semi-Annual Oscillations of the Fe and Na Layers

Another significant way in which the introduction of K_{dyn} modifies the metal layers is to reduce the dependence of the global distribution of metals on the horizontal transport by the residual meridional circulation, for which metals are transported toward the winter pole. This arises because of the shorter residence time of the metals above 80 km. The horizontal transport of metals has a clear annual cycle that can be studied by looking at the annual oscillation of the total column abundance anomalies for each metal. K_{dyn} also has a strong semi-annual cycle (according to Figure 2) that correlates with the semi-annual oscillation of the total column abundance anomalies.

Figure 6 shows the amplitude (Figures 6a and 6c) and the phase (Figures 6b and 6d) of the annual oscillation (AO) for the Fe and Na total column abundance monthly anomalies (computed against the annual mean) as a function of latitude for CTRL (dashed line) and K_DYN (solid line) (see also Methods, Section 3.1.2). For Na, the AO amplitude and phase derived from the observations (Figure 5) are also shown (note that for Fe a similar data set with global coverage is not available). The AO amplitude represents the largest value achieved by the oscillation at any point throughout the year, the AO phase represents the day of the year in which the amplitude is achieved.

The amplitude of the annual oscillation is smaller for K_DYN than for CTRL at all latitudes (Figures 6a and 6c). Differences maximize over the poles where the meridional transport largely influences metal densities. Here, the K_DYN AO amplitude for Fe and Na anomalies is at least twice as small as CTRL. Because of the larger downward vertical transport, and thus the shorter lifetime of the metals in the atmosphere, in K_DYN the metal concentrations depend less significantly on the strength of the horizontal transport (weaker AO), while in CTRL the metal layer is to a greater extent affected by the meridional convergence at high-latitudes in winter (stronger AO).

For both Na and Fe the phase of the annual oscillation diverges the most at low latitudes around the tropics, where the lag between CTRL and K_DYN can be as long as ∼200 days in the Southern Hemisphere (Figure 6b). This happens because the new total dynamical diffusivity K_{dyn} changes the way that the total column abundance anomalies vary throughout the year. As shown in Figure 2e, K_{dyn} has a strong seasonality. At 20°S, K_{dyn} is the largest during MAM and SON, leading to a larger vertical transport and thus smaller metal densities; conversely, K_{dyn} is the smallest during JJA (∼days 150–250), leading to greater metal densities. This seasonality results in a stronger (than horizontal transport) influence of K_{dyn} in determining the metal column abundance at low-latitudes. Note, however, that this is not an exhaustive explanation of how the new diffusivity might be affecting Fe and Na.

Metal atom densities also depend on changes in temperature and other constituents such as O, H, and O_3, and all of them are impacted by K_{dyn}. Thus, dynamical and chemical processes interact non-linearly with each other to determine the final metal density distribution.

In the comparison with observations, the amplitude of the Na annual oscillation in CTRL is confirmed to be too large, while the K_DYN AO amplitude is in closer agreement with the observations, although it is smaller than the observed values at almost all latitudes. Low to mid- southern latitudes are an exception in our analysis; here both CTRL and K_DYN underestimate the AO amplitude. Note, however, that as discussed in Section 4.2, this is the geographical region where the observational uncertainty is the largest. As for the AO phase, we note that observations at 20°S are in much better agreement with K_DYN than with CTRL. While one might be tempted to see in this result a confirmation of the role of K_{dyn} in altering the annual variation of Na, as discussed above, because of the low confidence in the observational products, this cannot be considered a conclusive proof.

4.3. CO_2, Temperature, and Gravity Wave Forcing Changes

We will see in this section that the K_DYN simulation is overall colder than CTRL almost everywhere in the MLT region. The K_DYN atmospheric cooling was found to be the combined result of at least three processes that we shall examine next in the following order: CO_2 radiative cooling, adiabatic cooling due to changes in the residual meridional circulation, and temperature diffusion by gravity waves. Of these three, CO_2 cooling and the increased diffusion of temperature by non-breaking and breaking gravity waves are directly induced by the new parametrization, while changes to the residual mean meridional circulation are the result of internal feedback coming from the model dynamics after the representation of the parametrized waves was modified.

The CO_2 atmospheric mixing ratio has a negative vertical gradient in the upper mesosphere and lower thermosphere (Figures 7a and 7b), thus an increase in diffusivity in the MLT region will cause more CO_2 to be mixed upwards. Figure 7 shows zonal mean cross-sections of CO_2 concentration, air temperature (T) and the expected temperature departure from radiative equilibrium $\left(-w^*\left(\frac{HN^2}{R}\right)\right)$ for June, Northern Hemisphere summer (see Figure S4 in Supporting Information S1 for Southern Hemisphere summer). This is when the mesosphere reaches its coldest temperature at high northern latitudes (Figures 7d and 7e), and when the largest atmospheric stability changes between K_DYN and CTRL occur, as we shall see next.

Note that the $-w^*\left(\frac{HN^2}{R}\right)$ term gives an estimate of how far the simulated zonal mean temperature $\left(\overline{T}\right)$ is driven away from the radiative equilibrium temperature $\left(\overline{T}_E\right)$ by the gravity waves according to the simplified Transformed Eulerian Mean (TEM) thermodynamic equation: $w^*\left(\frac{HN^2}{R}\right) = -\alpha\left(\overline{T} - \overline{T}_E\right)$, where w^* is the TEM vertical velocity, α is the radiative relaxation rate, H is the atmospheric density scale height.

In K_DYN, the increase in CO_2 concentration contributes to cool down the atmosphere between ~50–95 km at all latitudes (Figure 7f). The pattern of negative T anomalies correlates well with the pattern of positive CO_2 concentration anomalies (Figure 7c), with an asymmetry between the two hemispheres dictated by the latitudinal variation of the CO_2 vertical gradient. Atmospheric cooling is localized between ~70–95 km in the Northern Hemisphere, and extends down to 50 km in the Southern Hemisphere.

The mesospheric temperature anomalies in Figure 7f show that CO_2 cooling and the cooling/warming signal due to changes in the residual meridional circulation combine with opposite effects at high northern and southern latitudes. As discussed in more detail in Section 4.3.1 and 4.3.2, in K_DYN gravity waves drive a stronger residual meridional circulation than in CTRL (Figure S20 in Supporting Information S1) and thus a stronger adiabatic cooling/warming at high northern/southern latitudes (Figures 7g–7i). The adiabatic cooling at high northern latitudes at ≈85 km combines with the CO_2 cooling and amplifies the negative temperature anomalies. Conversely, at high southern latitudes the descending branch of the meridional circulation causes a stronger adiabatic warming that weakens the cooling deriving from an increase in CO_2. Note also that at all latitudes the diffusion of background temperature by breaking and non-breaking gravity waves, which will be discussed in Section 4.3.3, is also expected to be a contributor to the total atmospheric cooling shown in Figure 7f.

CO_2 cooling in the MLT contributes to change both the atmospheric stability and the meridional temperature gradient via introducing an asymmetrical cooling in the two hemispheres. Because of this, the circulation changes

between K_DYN and CTRL analyzed next are the result of two different forcing mechanisms: in the summer hemisphere, atmospheric stability changes dominate, altering the gravity wave forcing and thus leading to mesospheric wind changes; in the winter hemisphere, the atmospheric cooling that extends down to 50 km alters the stratospheric pole-to-Equator meridional temperature gradient and strengthens the SH westerly winter jet.

4.3.1. The Summer Hemisphere

We start by analyzing the response of the summer hemisphere. In the Northern Hemisphere, as stated previously, the atmosphere cools down in K_DYN between ∼70–95 km (Figures 7c and 7f). At these altitudes, the resulting denser atmosphere changes the atmospheric stability (represented by the squared Brunt-Väisälä frequency, N^2). Between ∼60–85 km, atmospheric cooling decreases the atmospheric stability by weakening the restoring buoyancy forces acting on an air parcel that moves upwards from the warmer layers below. Between ∼85–95 km atmospheric cooling makes the atmosphere much more stable; at 85 km the maximum negative temperature anomaly is achieved (i.e., at the summer mesopause) (Figure 7f) and above this altitude the vertical temperature gradient becomes positive as we transition into the thermosphere (Figures 7d and 7e). Thus, the buoyancy forces acting on an air parcel that moves upwards from the colder mesopause to the warmer thermosphere are much larger, and hence the K_DYN atmospheric stability is much larger than for CTRL.

This is illustrated in Figure 8 (see also Figure S7 in Supporting Information S1 for potential temperature profiles, and Figure S19 in Supporting Information S1 for cross-sections of N^2). At both middle and high latitudes, N^2 is about 30%–50% smaller for K_DYN than for CTRL, up to ∼80 km (Figures 8b and 8e). Above this altitude, N^2 increases for K_DYN and even doubles (100% increase in Figure 8e) compared to CTRL just below 90 km, the mesopause height.

The decrease/increase of atmospheric stability below/above the mesopause alters the gravity wave forcing in K_DYN by repressing wave breaking below the mesopause and favoring it above. In the limit of the saturated part of the wave spectrum (i.e., for waves that are approaching their critical levels), the enhanced saturation theory proposed by VanZandt and Fritts (1989) predicts that gravity waves are more prone to break as they approach atmospheric layers with a larger N (Fritts et al., 2004; VanZandt & Fritts, 1989; Whiteway, 1999). A larger N favors the growth of instability by increasing the vertical wave-number m, thus promoting fast oscillation ($m \rightarrow \infty$) and wave breaking as waves approach a critical level according to:

$$\hat{w}(z) = \hat{w}(z=0)e^{-imz}, \tag{19}$$

$$m = \frac{N}{(\bar{u} - c)}, \tag{20}$$

where $\hat{w}$ is the Fourier transform of the vertical velocity. Note that the equations above are valid under the assumptions that the flow is hydrostatic, adiabatic, irrotational and under the Boussinesq approximation. This is the same theory on which the WACCM gravity wave drag parametrization bases the computation of the wave stress and the saturation condition (Garcia et al., 2007). While Equation 19 is not explicitly computed within the model code, and is shown here to provide a physical understating of the mechanism at play, the dependence between N and the wave amplitude is embedded in the computation of the WACCM saturation stress (see Garcia et al., 2007, Equation A7), so that for larger N waves tend to saturate more easily.

In Figures 8c and 8f the wind tendencies associated with gravity wave breaking are smaller for K_DYN (solid black line) than CTRL (dashed black line) at those altitudes where $N^2_{K\_DYN} < N^2_{CTRL}$ (Figures 8a, 8b, 8d, and 8e). As $N^2_{K\_DYN}$ starts to increase and approaches N^2_{CTRL}, gravity waves become unstable and break in K_DYN since they have now reached their saturation amplitude. K_DYN wind tendencies become much larger than CTRL when $N^2_{K\_DYN} \sim N^2_{\mathrm{CTRL}}$ (at ∼80 and 83 km at 40°N and 60°N, respectively) and remain larger above this height up to about 85 km at 40 N and 90 km at 60°N. At these altitudes, $N^2_{K\_DYN} \gg N^2_{CTRL}$ and wave breaking is favored in K_DYN according to Equations 19 and 20. Because more waves dissipate in K_DYN between 80 and 90 km, K_DYN wind tendencies become smaller than the CTRL ones just above the mesopause (∼90 km): in K_DYN these waves have been dissipated at lower altitudes.

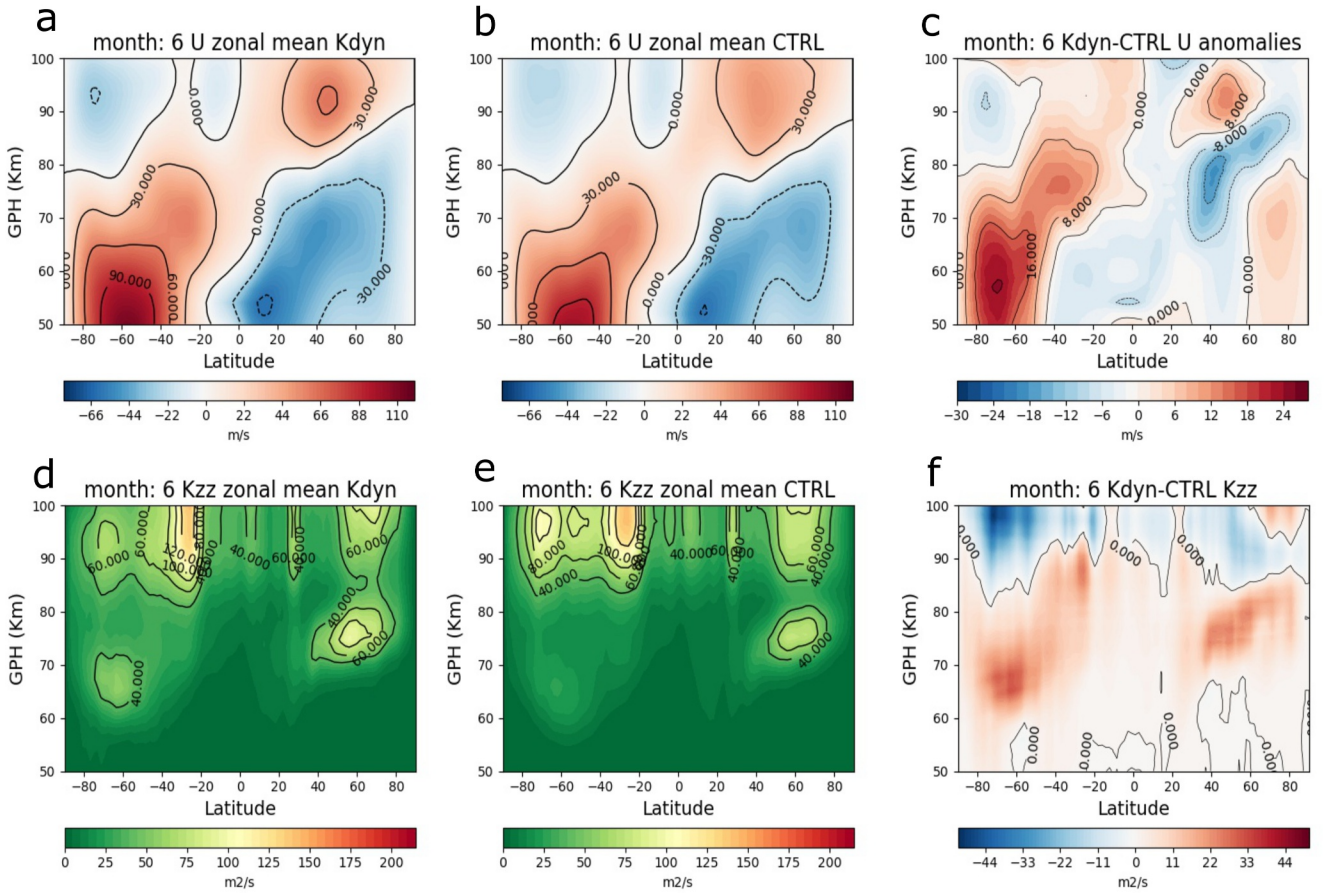

Figure 9. Zonal mean cross-sections of zonal wind (U) and eddy diffusivity (K_{zz}) simulated by K_DYN (a, d), CTRL (b, e) and their anomaly (c, f) for Northern Hemisphere summer conditions (June).

We stress that a full explanation of wind tendency changes should take into account that waves will also break differently in response to changes in the wind speed via critical level filtering. The flow behavior discussed above is consistent with atmospheric stability changes and is detectable at both middle and high latitudes; however, the signal can be stronger or weaker at heights where additional wave dissipation mechanisms might be active (see, for example, regions between 70 and 75 km and above 90 km).

In summary, for K_DYN we observe an upward shift of the wave breaking location due to changes in N^2 below and above the mesopause. We also observe an overall increase in the strength of the gravity wave forcing between ~80–90 km, because more waves break at these altitudes due to the larger N^2. As expected, the increase/decrease in wind tendencies below/above ~85–90 km is mirrored by the K_{zz} anomaly field shown in Figure 9f.

Changes in gravity wave forcing are reflected by circulation changes. The K_DYN mesospheric jet is higher and stronger (because of the larger positive wind tendencies) than in CTRL (Figures 9a–9c). In Figures 8c and 8f the major contributor to the total wind tendencies (black line) are fast eastward traveling gravity waves (red line) with a positive phase speed greater than 40 ms^{-1}. The upward shift of the location where these waves exert their forcing on the background flow means that the wind reversal from easterly to westerly occurs at higher altitudes in K_DYN than in CTRL, and the zero-wind line moves upwards (see dipole of anomaly at mid- to high northern latitudes in Figure 9c). The large positive anomaly of the eastward momentum flux between 75 and 85 km in the Northern Hemisphere confirms the height shift of the wind reversal for K_DYN (Figure S8c in Supporting Information S1).

A final note on the wind changes of Figure 9c in the Northern Hemisphere is that, at about 70 km, the easterly jet is stronger in K_DYN than CTRL (negative anomalies). This is again consistent with less eastward-traveling

gravity waves breaking at these altitudes (smaller wind tendencies in Figure 8). By carrying eastward momentum flux, the dissipation of these waves would indeed cause the easterly winds to decelerate.

The stronger mesospheric jet in K_DYN is related to a stronger residual mean meridional circulation from the summer to the winter hemisphere (Figure S20 in Supporting Information S1). The larger momentum flux divergence by gravity wave breaking near the mesopause causes a stronger vertical ascending motion, and thus a stronger adiabatic cooling (Figures 7g and 7h). Because of the upward shift of the wind reversal, the adiabatic cooling extends higher up in the atmosphere and in K_DYN the mesopause height shifts upwards too (86 km for K_DYN vs. 83 km for CTRL) (see also Section 4.4.2). The largest negative temperature anomalies between K_DYN and CTRL are attained at the summer polar mesopause (Figure 7f), this is where the CO_2 radiative cooling and the dynamical adiabatic cooling combine, as discussed in Section 4.3.1.

As the mesospheric meridional circulation strengthens, due to mass continuity, the corresponding meridional circulation cell in the thermosphere (directed in the opposite direction) strengthens too. This circulation is characterized by a descending air motion, and thus adiabatic warming, in summer. In Figure 7f above 95 km K_DYN temperatures are larger than CTRL because of the additional warming associated with a stronger lower thermospheric residual circulation.

It is important to highlight, at this point, that the primary drivers behind the stability changes discussed in this section are those processes that are directly modified by the introduction of the new diffusivity K_{Dyn}, that is, the diffusion of background temperature (see next section) and constituents like CO_2 that will cool down the atmosphere. These processes must be responsible for altering the gravity wave drag, according to the analysis presented above, since the new parametrization does not modify the way the wave stress and its divergence are computed in WACCM (see Section 2.2.1). It follows, that the changes in adiabatic cooling/warming described above and discussed in Section 4.3.1 (Figures 7g and 7h) are a secondary effect arising from the dynamical response of the model to the atmospheric cooling promoted by a larger K_{Dyn}. This also implies that a positive feedback must be active within the model as a colder and higher mesopause, once established, will only strengthen the atmospheric stability changes discussed above.

4.3.2. The Winter Hemisphere

In the Southern Hemisphere, CO_2 cooling extends to lower atmospheric layers and affects the stratosphere (Figure 7c). The lower atmosphere does not cool down uniformly, the cooling is stronger at high latitudes with negative temperature anomalies extending down to 50 km and weaker at mid- to low latitudes. The differential cooling between high and low latitudes alters the stratospheric pole-to-Equator meridional temperature gradient (making it stronger). Because of thermal wind balance, a stronger meridional temperature gradient drives a much stronger ($\sim$+20 ms^{-1}) stratospheric westerly jet for K_DYN compared to CTRL above 50 km (Figure 9c).

Unlike circulation changes in the Northern Hemisphere, the stronger winter hemisphere westerly jet cannot be explained by atmospheric stability changes. In the winter hemisphere atmospheric stability changes are modest, with a maximum decrease of $N^2_{K\_DYN}$ of about 20% at 65 km (see Figure S9a in Supporting Information S1) where the vertical temperature gradient is strongly affected by CO_2 cooling (Figure 7c). Although similar to what happens in the Northern Hemisphere, the increase in K_{zz} between 80 and 40°S and 60–70 km (Figure 9f) can be explained by a smaller N^2 for K_DYN compared to CTRL (Figure S9 in Supporting Information S1), the larger wind tendencies for K_DYN are associated with westward traveling gravity waves (Figure S9b in Supporting Information S1). These waves have a negative phase speed and, as they break, act to decelerate the westerly jet (see also Figure S8f in Supporting Information S1 which shows the corresponding positive anomaly in westward momentum flux). However, as explained above, the dominant mechanism at these latitudes for the stratospheric jet intensification is the stronger meridional temperature gradient, so the overall Southern Hemisphere westerlies are stronger in K_DYN than CTRL.

Finally, note that while the analysis above mainly focused on the Northern Hemisphere summer/Southern Hemisphere winter, for the Southern Hemisphere summer/Northern Hemisphere winter similar conclusions can be drawn. The same variables shown in Figures 7–9 are shown in Figures S4–S6 in Supporting Information S1 for December.

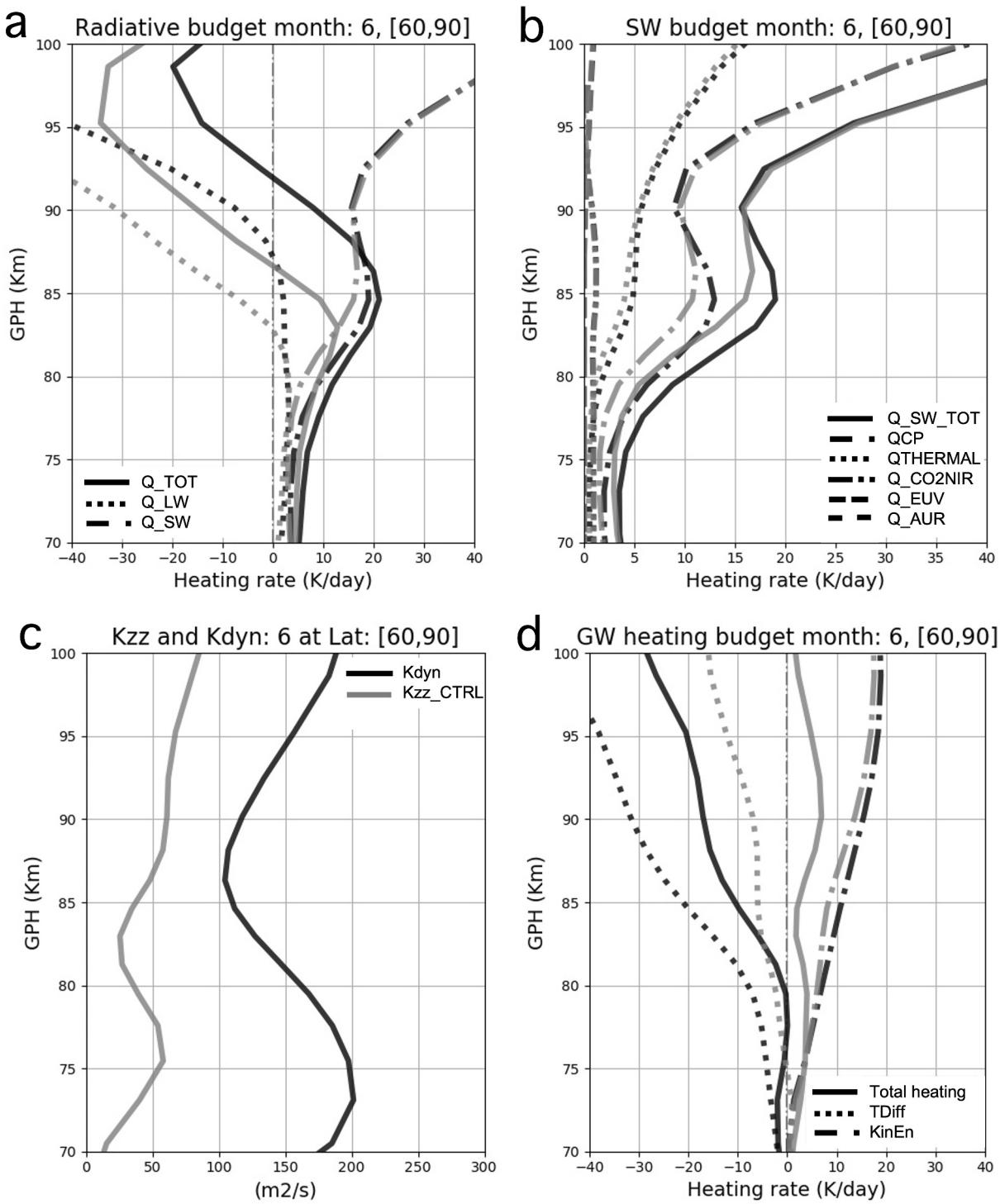

Figure 10. Vertical profiles of total radiative heating budget (a), short-wave radiation budget (b), K_{zz}_CTRL and K_{Dyn} (c), and gravity wave heating budget (d) for K_DYN (black line) and CTRL (gray line) for Northern Hemisphere summer conditions (June) between 60°N and 90°N.

4.3.3. Radiative and Gravity Wave Heat Budget

We next analyze the effects of a larger diffusivity coefficient on the radiative heating rates in the MLT region, and how these compare with changes in the gravity wave-induced heating. In the light of the discussion above, we focus our analysis on Northern Hemisphere high latitudes during the summer season, where K_DYN versus

CTRL anomalies are the largest. The processes discussed in this section for high latitudes dominate the global temperature response (except for the chemical potential heating rate, see below). The global means of the variables shown in Figure 10 are presented in Figure S11 in Supporting Information S1, for completeness.

In Figure 10a the total radiative heating budget (given by the sum of short-wave heating plus long-wave heating) for K_DYN (black solid line) and CTRL (gray solid line) between 60 and 90°N and 70–100 km for June is shown. Above ∼80 km the total radiative heating (Q_{TOT}) is more positive for K_DYN than for CTRL (solid black and gray lines, respectively). This is the consequence of the short-wave heating term (Q_{SW}, dash-dotted line) being larger (∼3 K day^{-1}) and of the long-wave heating term (Q_{LW}, dotted line) becoming negative for K_DYN at higher altitudes (at 87 km rather than 83 km for CTRL), with the latter being the major contributor to the total anomaly.

In the MLT region, long-wave heating rates are mostly negative throughout the year except near the polar summer mesopause (Akmaev & Fomichev, 1998; López-Puertas & Taylor, 2001; Portmann et al., 1995). In K_DYN, the colder and higher mesopause (in accordance with the upward shift of the mesospheric jet discussed above) makes the long-wave forcing change from positive to negative at higher altitudes than in CTRL, contributing to the overall larger total radiative heating rate.

To understand changes in the short-wave heating rate, we need to look at the different heat sources that contribute toward it (Figure 10b). The short-wave heating rate is the sum of heat coming from the recombination of photolysis products (the chemical potential heating rate, *QCP*), direct absorption of solar radiation (*QTHERMAL*), extreme UV heating (Q_{EUV}), CO_2 near infra-red absorption (Q_{NIR}), and heat due to particle precipitation during auroras (Q_{AUR}). As shown in Figure 10b, differences in the K_DYN and CTRL total short-wave heating rate are solely the result of a change in the chemical potential heating rate. *QCP* (dash-dotted line) is much larger for K_DYN (∼3 K day^{-1}) between 80 and 85 km. This is the result of more atomic oxygen (O) being transported downwards in K_DYN from the thermosphere (Figure S10c in Supporting Information S1), where it is formed by photo-dissociation of O_2. A larger concentration of atomic oxygen means that more exothermic reactions take place at these altitudes, increasing the total Q_{SW}. Note, however, that this is a localized (high-latitude) response. In fact, positive O anomalies at ∼80–85 km correspond to negative O anomalies in the atmospheric layers above (Figure S10c in Supporting Information S1). In the *QCP* global mean (Figure S11 in Supporting Information S1), negative anomalies dominate the signal above ∼85 km and the overall decrease of K_DYN atomic oxygen makes the short-wave heating rate smaller in K_DYN for the global atmosphere above this height (Figure S11 in Supporting Information S1).

In Figure 10d the total gravity wave heating budget is shown. This represents the way in which breaking (for CTRL) and breaking + non-breaking (for K_DYN) gravity waves directly affect the thermal structure of the atmosphere. The gravity wave heating rate is always positive for CTRL (solid gray line) and mostly negative for K_DYN (solid black line). The change in the sign of the gravity wave forcing is a consequence of the larger thermal diffusion at all altitudes for K_DYN introduced by the larger diffusivity coefficient (i.e., $K_{Dyn} \gg K_{zz}$), as explained below. When waves dissipate, the energy lost by the waves represents a heat source for the background flow. This heating rate is always positive (KinEn term, dash-dotted line in Figure 10d), since it represents the conversion of kinetic energy into heat via turbulent dissipation, and above 80 km is larger for K_DYN than CTRL because of the stronger dissipation of waves at these altitudes (see Figures 9b and 9e). In contrast, the modeled vertical diffusion of temperature due to gravity wave mixing is always negative (TDiff term, dotted line in Figure 10d). This term strongly depends on the magnitude of eddy diffusivity coefficient K_{zz}. In the WACCM gravity wave drag parametrization, eddy heat fluxes are computed as follows (Garcia et al., 2007):

$$\overline{w'\vartheta'} = -K_{zz}\frac{\partial\overline{\theta}}{\partial z}. \tag{21}$$

Hence, for a statically stable atmosphere $\left(\frac{\partial\overline{\theta}}{\partial z} > 0\right)$, this term is always negative and represents the upward mixing of colder air.

For CTRL, temperature diffusion depends only on the strength of the mixing induced by breaking gravity waves (K_{zz}_*CTRL*). For K_DYN, the vertical diffusion of temperature is affected by the mixing associated with breaking and non-breaking vertically propagating gravity waves (K_{Dyn}). Thus, for K_DYN, K_{Dyn} replaces K_{zz} in

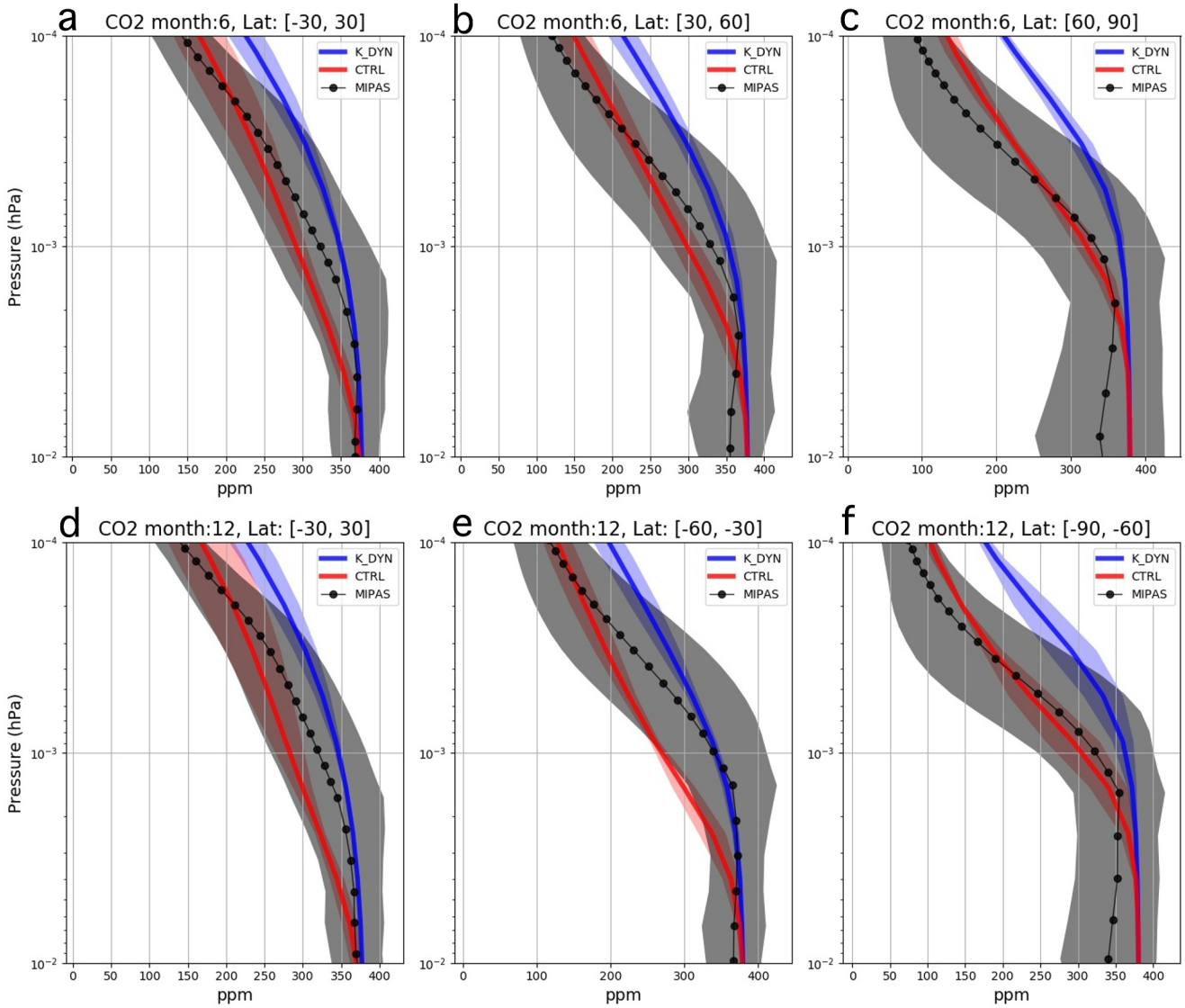

Figure 11. Vertical profiles of CO_2 mixing ratio for June in the Northern Hemisphere (a, b, c) and December in the Southern Hemisphere (d, e, f) (i.e., summer solstice conditions) for MIPAS observations (black dots), K_DYN (blue line) and CTRL (red line) for years 2008–2011. Area-weighted means were computed over the tropics (a, d), mid-latitudes (b, e) and polar regions (c, f). Shaded areas correspond to two times the standard deviation of the spatial mean for both modeled and observed data.

Equation 21. Since K_{Dyn} is everywhere larger than K_{zz}_CTRL (Figure 10c), the heating rate representing temperature diffusion by gravity waves is larger (and more negative) in K_DYN than in CTRL according to Equation 21 (Figure 10d).

The analysis above reveals that there is an additional cooling mechanism that contributes, together with the increase in CO_2 and the adiabatic cooling discussed above, to the observed negative temperature anomalies: the larger temperature diffusion due to breaking + non-breaking gravity waves. As discussed in Section 2.2, while the diffusion of temperature by both breaking and propagating gravity waves is expected to be larger than diffusion produced only by breaking waves, it is apparent that the new diffusivity (K_{Dyn}) diffuses temperature too strongly in the current code implementation. In Section 5 we discuss this point further and suggest possible ways to improve the model.

4.4. CO_2 and Air Temperature Model-Observations Comparisons

In this section we analyze how the WACCM model with the new wave-transport parametrization compares to its standard configuration when simulating mesospheric CO_2 and temperature. We compare K_DYN and CTRL against MIPAS satellite observations for the period 2008–2011.

4.4.1. CO_2

López-Puertas et al. (2017) found that, while the WACCM model simulates correctly the CO_2 seasonal change and latitudinal distribution, it tends to underestimate mesospheric CO_2 concentrations particularly at middle to low latitudes between ∼90–100 km for summer solstice conditions, and overestimate CO_2 concentrations for autumn equinox conditions above ∼100 km at almost all latitudes. Figure 11 shows MIPAS (black dots), CTRL (red line), and K_DYN (blue line) CO_2 concentrations for Northern Hemisphere (June) and Southern hemisphere (December) summer solstice conditions. Figure 12 shows the same fields but for autumn equinoxes (September and March).

As discussed in Section 4.3, the mixing induced by propagating gravity waves increases the CO_2 concentration everywhere in the upper MLT region compared to CTRL. The K_DYN larger CO_2 concentration significantly improves, and at times cancels, the model bias at middle and low latitudes for summer solstice conditions between $\sim10^{-2}$–10^{-3} hPa (∼80–90 km) (Figures 11a, 11b, 11d, and 11e). Above $\sim10^{-3}$ hPa however, K_DYN over-compensates the CO_2 under-representation in CTRL and overestimates CO_2. At these altitudes, the CTRL and K_DYN simulated means both lie between twice the standard deviation of the observational mean, making it difficult to unequivocally determine which model version performs better. For altitudes near 100 km ($\sim10^{-4}$), and at high-latitudes everywhere (Figures 11c–11f), K_DYN overestimates CO_2.

K_DYN compares similarly with MIPAS at the equinoxes (Figure 12). However, for middle and low latitudes CO_2 is to some extent always overestimated by K_DYN, particularly above $\sim10^{-3}$ hPa (Figures 12a, 12b, 12d, and 12e). At high latitudes, CO_2 concentration is now better represented by K_DYN below $\sim10^{-3}$ hPa (Figures 12c and 12f).

From the analysis of Figures 11 and 12 we can see that the increase in atmospheric CO_2, promoted by the larger dynamical diffusivity K_{Dyn}, means that in K_DYN model-observations agreement is often improved in regions where CO_2 is underestimated by CTRL below $\sim10^{-3}$ hPa, but worsened in regions where CTRL overestimates CO_2 (e.g., at the equinoxes, and for altitudes near 100 km $\sim10^{-4}$ hPa). We also conclude that, in general, K_DYN tends to simulate too high CO_2 concentrations even in regions where CTRL underestimates them. Reasons for the CO_2 overestimation are discussed in Section 5.

In summary, although we found that K_DYN tends to overall overestimate mesospheric CO_2 concentrations, our results support previous studies that found that the representation of CO_2 in the WACCM model is highly sensitive to the magnitude of the eddy diffusivity associated with gravity waves in the MLT region (e.g., Garcia et al., 2014; Garcia et al., 2016). Remarkably, while Garcia et al. (2016) used sensitivity tests in which the model K_{zz} was artificially increased to obtain a satisfactory model-observations agreement, our wave-induced constituent transport parametrization introduces a missing process within the model physics that increases atmospheric CO_2 dynamically.

4.4.2. Temperature

The K_DYN temperature field responds to changes in CO_2 concentration, temperature diffusion by gravity waves and, at high latitudes, in the residual meridional circulation (see Section 4.3 for details). We compared the K_DYN and CTRL simulated air temperature with MIPAS retrievals at high (90°N/S and 60°N/S), middle (40°N/S) and low (20°N/S) latitudes. Figure 13 shows comparisons for 40°N and 40°S, and the high and low latitude comparisons are shown in Supplementary (Figures S12–S17 in Supporting Information S1). We can see that K_DYN is colder than CTRL at all latitudes and altitudes, and that model-observations agreement is degraded. Often, however, MIPAS observations sit between the K_DYN and CTRL estimates, indicating that while CTRL has a warm bias for mesospheric temperatures, K_DYN tends to overcompensate this bias by cooling down the mesosphere too much. As expected, K_DYN agrees better with MIPAS than CTRL when the latter overestimates temperatures significantly. The reverse happens (K_DYN largely underestimates observations) when CTRL estimates are closer to MIPAS observations.

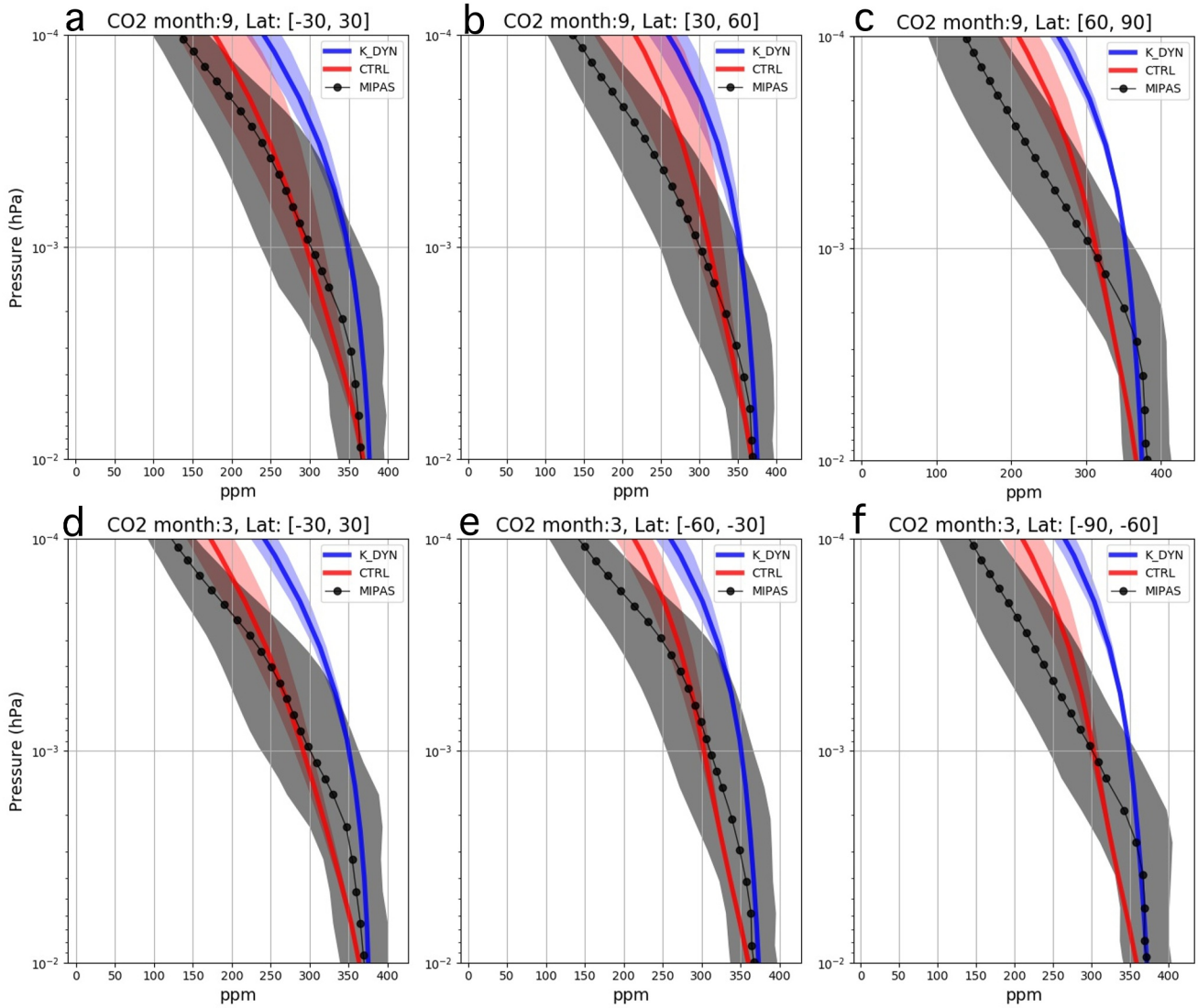

Figure 12. As for Figure 11 but for September in the Northern Hemisphere (a, b, c) and March in the Southern Hemisphere (d, e, f) (i.e., autumn equinox conditions).

At high latitudes for spring seasons model-observation comparisons improve for K_DYN at ~10^{-3} hPa (and below). Overall, K_DYN performs better than CTRL in estimating spring polar temperatures at both 60 and 80°N in April/May (Figures S14 and S16 in Supporting Information S1), and at 60 and 80°S in October/November (Figure S15 and S17 in Supporting Information S1). For these spring months, we note that the large warm bias of CTRL is largely reduced or, at times, totally removed. Model-observations agreement for K_DYN worsens significantly in summer in both hemispheres, owing to the additional role played by the K_DYN stronger meridional circulation. The summer mesopause as represented by K_DYN is too cold by ~30K compared to MIPAS, while CTRL here provides a better agreement although retaining a positive (warm) bias of about 10K. As discussed in Section 4.3.1, besides the stronger adiabatic cooling, another consequence of the stronger residual meridional circulation in K_DYN is a higher summer mesopause height. When compared with observations (Figure 14), this yields an improvement in the polar summer mesopause height (defined as the coldest point): in the Northern Hemisphere, MIPAS and K_DYN indicate both a mesopause at ~86 km against the CTRL mesopause height of ~83 km. In the Southern Hemisphere, the MIPAS, K_DYN and CTRL mesopause heights are ~90, 87, and 84 km, respectively. Finally, we note that the upward shift of the mesopause in K_DYN results in temperatures at and just above the MIPAS coldest point (~90–95 km in Figure 14) that are represented better in K_DYN than CTRL (see also Figue S1 in Supporting Information S1).

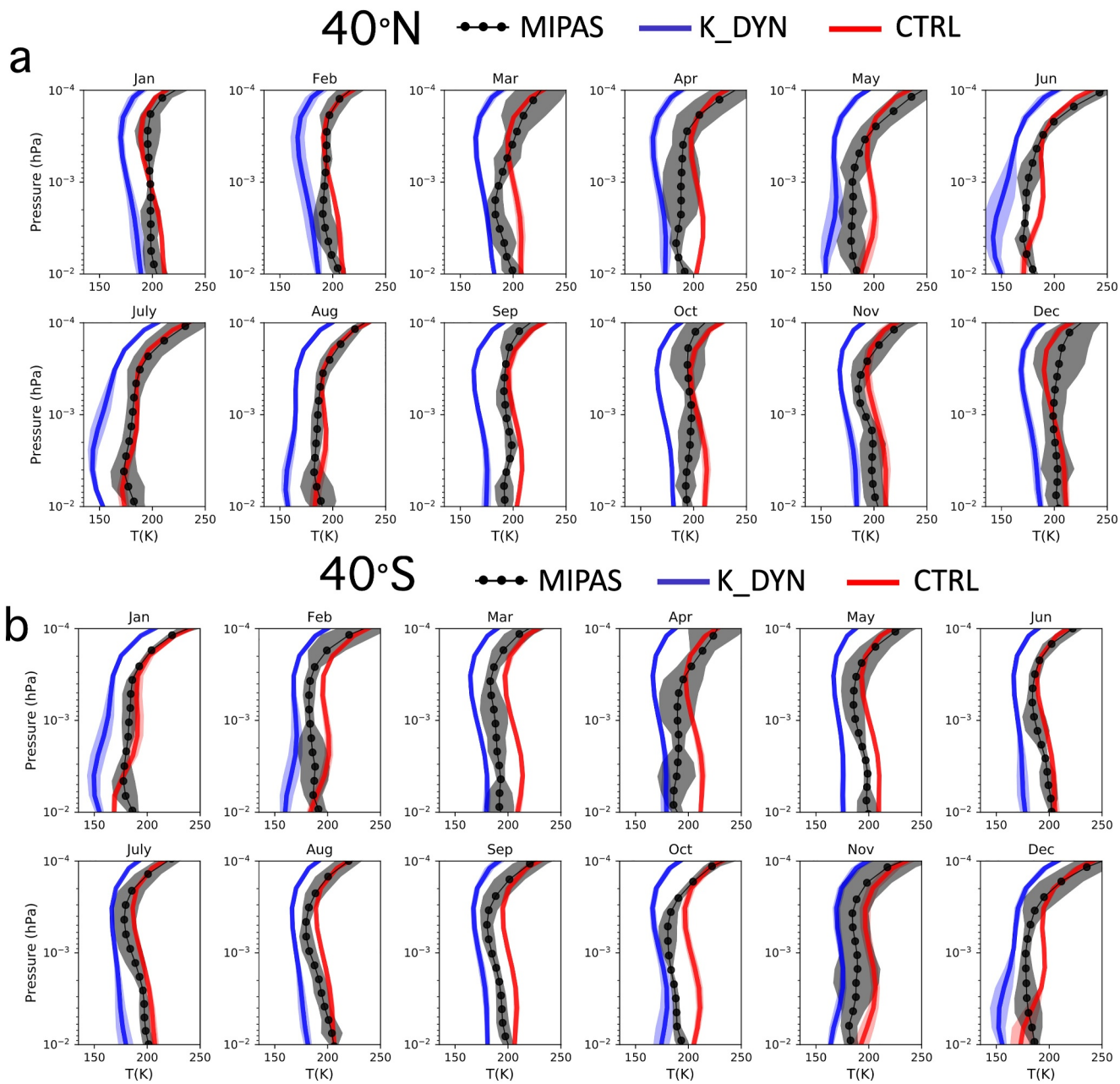

Figure 13. Monthly vertical temperature profiles for MIPAS observations (black dots), K_DYN (blue line) and CTRL (red line) for years 2008–2011 at 40°N. Shades represent two times the standard deviation of the temporal means for both modeled and observed data.

5. Conclusions and Final Remarks

A new gravity wave transport parametrization has been implemented in the Whole Atmosphere Community Climate Model (WACCM). The parametrization is based on a novel theory that allows us to represent the diffusion of atmospheric constituents by propagating, non-breaking, gravity waves via the effective wave diffusivity (K_{wave}). Using K_{wave}, a new total dynamical diffusivity (K_{Dyn}) is defined. K_{Dyn} represents the vertical mixing of the atmosphere by both breaking (dissipating) and vertically propagating (non-dissipating) gravity waves. In the new parametrization, K_{Dyn} replaces the eddy diffusivity K_{zz} in the WACCM gravity wave scheme and is used to diffuse both atmospheric constituents and background temperature.

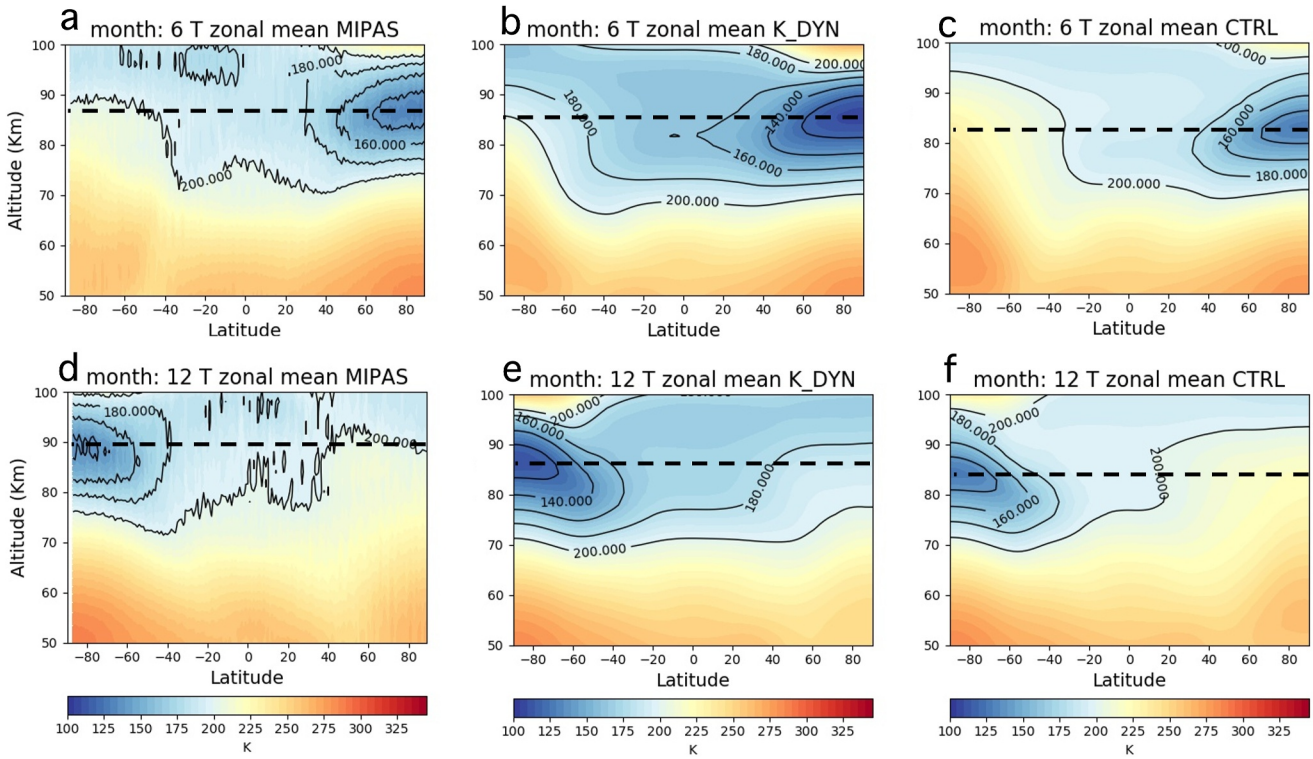

Figure 14. Zonal mean temperature for MIPAS (a, d), K_DYN (b, e) and CTRL (c, f) for June (top panels) and December (bottom panels). Dashed lines represent the height of the polar summer mesopause (defined as the height of the coldest temperature).

This is the first time that a parametrization for the wave mixing by propagating non-breaking gravity waves has been implemented in a global chemistry-climate model. Non-dissipating gravity waves contribute to the total mixing of the atmosphere inside and outside dissipation regions, thus gravity waves have an impact on the background flow even if they do not dissipate. This is a major difference with traditional dissipative-only gravity wave parametrizations.

The WACCM model with the new gravity wave mixing parametrization (K_DYN) was compared against a model version using the standard gravity wave drag parametrization (CTRL), and against observations for Na, Fe, mesospheric CO_2 and temperature. Lidar measurements for Na and Fe come from three observational sites located at middle and high latitudes, these are: Urbana (40°N, 88°W), Rothera (68°S, 68°W) and South Pole (90° S). For CO_2 and temperature, we used MIPAS_V8 satellite retrievals. We focused our analysis on the 2008–2011 period.

Model-observation comparisons showed that when gravity wave transport is included (K_DYN simulation) the model's ability to simulate the metal layers significantly improves: MIFs that are within a factor of 2 of the most recent estimates (Carrillo-Sánchez et al., 2020; Hervig et al., 2021) can now be used in WACCM. While Fe and Na concentrations between ∼80–100 km are largely overestimated by CTRL (up to more than double their observed densities), K_DYN provides a greatly improved model-observations agreement. The introduction of the new dynamical diffusivity alters the extent to which Fe and Na concentrations are influenced by the horizontal transport operated by the residual mean meridional circulation (directed from the summer pole to the winter pole). The AO amplitude is smaller in K_DYN than in CTRL because of the shorter lifetime of the metals in the atmosphere. At the same time, we found that K_{dyn} introduces a stronger semi-annual oscillation in the Fe and Na column abundance variation over the year.

Regarding mesospheric CO_2, K_DYN model-observations agreement is overall improved between 80 and 90 km in regions where CTRL is known to significantly underestimate CO_2 (i.e., middle and low latitudes during summer solstices). At the same time, however, model-observations agreement worsens in regions where CTRL

overestimates CO_2 because in these regions K_DYN exacerbates the model bias (e.g., at equinoxes, and for altitudes near 100 km). A too large CO_2 concentration means that in K_DYN the CO_2 radiative cooling is excessive.

We analyzed the global temperature field between 70 and 100 km and found that while CTRL has a warm bias in representing the MLT region, particularly between 70 and 90 km (~10-2–10-3 hPa), K_DYN overcompensates for this warm bias. We thus conclude that the mesospheric cooling currently simulated by K_DYN, while needed, is currently too strong almost everywhere. An exception to the above conclusions is represented by high latitude spring temperatures; these are better simulated by K_DYN than CTRL. Additionally, in K_DYN the polar summer mesopause height shifts upwards providing a better match with the observed MIPAS mesopause height, correcting the too low CTRL mesopause height in the Northern Hemisphere and improving it in the Southern Hemisphere. Note however that, in terms of temperature structure, the K_DYN mesopause temperature is too cold compared to MIPAS (~−30K), while CTRL, although simulates a too low mesopause, gets closer (~+10K) to the observational estimate.

The K_DYN atmospheric cooling was found to be dominated by three different mechanisms: (a) radiative cooling by CO_2, (b) adiabatic cooling due to a stronger meridional residual circulation, and (c) temperature diffusion by gravity waves.

Of these three, CO_2 cooling and the increased temperature diffusion by gravity waves are directly induced by the new parametrization, while changes to the residual mean meridional circulation are the result of internal model feedbacks following the updated representation of the parametrized waves.

Complex atmospheric stability and circulation changes take place in the model when K_{Dyn} is introduced. Results on circulation changes can be summarized as follows: in K_DYN the atmosphere cools down at all latitudes compared to CTRL. Importantly, the pattern of CO_2 cooling introduces an asymmetry between summer and winter hemisphere. In the summer hemisphere, N^2 is smaller just below the mesopause and larger just above. In K_DYN gravity waves break at higher altitudes, and with larger amplitudes, compared to CTRL owing to the dependence of their saturation amplitude on N^2. This causes the residual meridional circulation to strengthen. The resulting stronger upwelling motion is accompanied by a stronger adiabatic cooling. The combination of CO_2 cooling and adiabatic cooling causes the negative temperature anomalies to maximize at the summer mesopause. In the winter hemisphere, the atmosphere near 50 km cools down more strongly at high latitudes than lower latitudes. The differential cooling between pole and Equator alters the meridional temperature gradient. Because of the stronger gradient, the Southern Hemisphere westerly winter jet strengthens.

In K_DYN the background temperature is diffused by both breaking and non-breaking gravity waves (diffusivity coefficient in the temperature diffusion equation: K_{Dyn}), compared to CTRL where temperature is diffused by breaking gravity waves only (diffusivity coefficient: K_{zz}). Since K_{Dyn} is larger than K_{zz} always, temperature is diffused more strongly in K_DYN than CTRL. Net gravity wave heating is thus negative in K_DYN and contributes to cooling down the atmosphere. We point out that while it is expected that the diffusion of the background temperature by both breaking and propagating gravity waves be larger than the diffusion by K_{zz} alone (as in CTRL), the temperature diffusion by K_{Dyn}, as currently implemented in the mode code, is too large (Section 2.2). This is one reason why K_DYN temperatures are too cold compared to observations. Future work on the new parametrization presented here will allow us to refine the current formulation of constituent and temperature diffusion by gravity waves. We will use a new updated theoretical formulation for K_{Dyn} and K_H that takes into account the compressibility of the wave perturbations (currently assumed to be incompressible, Gardner et al. (2019)). Theoretical predictions indicate that the new expression for the thermal diffusivity is much smaller than the K_{Dyn} used in this study but it is larger by about 50% or more than K_{zz}. We therefore expect that gravity waves will still diffuse temperature more than CTRL but less strongly, and that the model cold bias will be reduced.

A second reason why the new parametrization simulates a too cold atmosphere compared to observations is the CO_2 overestimation in the MLT region, as discussed above. CO_2 cooling was found to be a major driver of the radiative cooling in K_DYN. Tests were carried out by studying the evolution of the CO_2 radiative forcing time-step by time-step (Text S1 in Supporting Information S1). This was necessary to remove the dependency of the CO_2 cooling rate on the background temperature. CO_2 cooling was responsible for cooling down K_DYN compared to CTRL with a rate of about 15 K day^{-1} in one single time-step. An additional, but more modest

(~3 K day^{-1}), source of cooling was also identified to come from a decrease in atomic oxygen concentration above ~85 km (see Section 4.3.3).

The overestimation of CO_2 concentration in the MLT region, particularly at high altitudes (above 10^{-3} hPa, ~90 km) where gravity wave amplitudes are large, indicates that the new parametrization requires some tuning in the strength of the K_{Dyn} diffusivity, which may also be too large owing to the underlying treatment of gravity waves in the WACCM gravity wave drag parametrization. As discussed in Section 2.2, the WACCM gravity wave amplitudes tend to become unrealistically large as the waves propagate upwards. The introduction of a wave damping was necessary to get reasonable value of K_{wave}, and hence K_{Dyn}. In some instances, we also found that a few fast-traveling gravity waves are not dissipated within the model vertical column and keep on propagating upwards reaching the model top. These same waves are the ones for which the wave damping can be weakly effective (i.e., high-frequency, short-period gravity waves). Therefore, it is likely that a combination of the default WACCM gravity wave source spectrum and the efficiency of the wave damping introduced here contribute to make K_{Dyn} too large at high atmospheric levels.

Considering the above, tuning the strength of the new dynamical diffusivity can be done by, for example, refining the wave damping. However, it is worth pointing out that while a smaller K_{Dyn} would improve CO_2 model-observation comparisons (and the associated cooling), at the same time, a smaller dynamical diffusivity will change the modeled Fe and Na densities. This highlights the complexity of the tuning of model parametrizations, which becomes a balancing act between accurate physical representation and acceptable model skill. Of course, waves also induce a chemical flux, which is important for chemically active species like Na and Fe but was not included in K_DYN. Wave-induced chemical effects for key species need to be included in the future versions of the model as they will impact tuning of the parametrization.

To conclude, in this study we have shown that the role of gravity waves in influencing the atmospheric physics and chemistry goes well beyond the sole impact of gravity wave drag due to wave dissipation. In that sense, the current gravity wave treatment and representation in state-of-the-art global chemistry-climate models is incomplete as it ignores non-dissipative processes. We presented here the first implementation of a new wave-driven transport parametrization. This constitutes a starting point that will allow us to improve the model tuning and refine the theory in order to obtain a much improved representation of the upper layers of the Earth's atmosphere.

Appendix A: A Model for ξ_{inst}

Var(T') and Var($\partial T'/\partial z$) are related through their vertical wavenumber spectra. Extensive observations have shown that the vertical wavenumber spectra of the horizontal wind and temperature fluctuations follow a power-law of the form m^{-q} in the region $m_* < m$, where $q \approx 3$ and $m_* = 2\pi/\lambda_z^*$ is the characteristic vertical wavenumber (e.g., Gardner, 1996). Several theories predict that $q = 3$ and $m* \sim N/u'_{rms} \sim (\Gamma_{as} + \partial T/\partial z)/T'_{rms}$. Furthermore, these theories predict that the m-spectrum magnitude for $m_* < m$ remains approximately constant with altitude so that as the wave field propagates upward, m_* decreases to accommodate the increasing variances of u' and T'. If the wave u' amplitudes are limited by shear and convective instabilities to values on the order of N/m, then the m-spectrum of the temperature fluctuations is

$$F_{T'}(m) = 2\pi\gamma \begin{bmatrix} \dfrac{\left(\Gamma_{ad} + \partial\overline{T}/\partial z\right)^2 m}{m_*^4} & 0 \le m \le m_* \\ \dfrac{\left(\Gamma_{ad} + \partial\overline{T}/\partial z\right)^2}{m^3} & m_* \le m \le m_b \end{bmatrix} \tag{A1}$$

The wavenumber $m_b = 2\pi/\lambda_b$ marks the transition between waves and turbulence, where $\lambda_b \sim 1$ km. The parameter $\gamma \sim 1/8$ is determined by comparing the model spectrum magnitude in the region $m_* < m$ to measured spectra. Computing the T' and $\partial T'/\partial z$ variances using Equation A1 yields

$$\frac{\mathrm{Var}\left(T'\right)}{\left(\Gamma_{\mathrm{ad}} + \partial\overline{T}/\partial z\right)^2} = \frac{\gamma}{m_*^2}\left[1 - 0.5\left(\frac{m_*}{m_b}\right)^2\right] \quad m_* \le m_b \tag{A2}$$

$$\frac{\mathrm{Var}\left(\partial T'/\partial z\right)}{\left(\Gamma_{\mathrm{ad}}+\partial\overline{T}/\partial z\right)^2}=\xi_{inst}=\gamma\left[\frac{1}{4}+\ln\left(\frac{m_b}{m_*}\right)\right]\quad m_*\le m_b \tag{A3}$$

and

$$\lambda_z^*=2\pi\sqrt{\frac{\mathrm{Var}\left(T'\right)}{\alpha\left(\Gamma_{\mathrm{ad}}+\partial\overline{T}/\partial z\right)^2}+\frac{1}{2m_b^2}} \tag{A4}$$

Substituting Equation A4 in A3 gives

$$\xi_{inst}=\frac{\gamma}{4}+\frac{\gamma}{2}\ln\left[\frac{(2\pi)^2}{\gamma\lambda_b^2}\frac{\mathrm{Var}\left(T'\right)}{\left(\Gamma_{ad}+\partial\overline{T}/\partial z\right)^2}+\frac{1}{2}\right] \tag{A5}$$

Gamma (γ) is tunable parameter that can be determined from theory or atmospheric observations. It is well-known that in the presence of a spectrum of waves, shear and convective instabilities will limit individual wave T' amplitudes to $\epsilon\left(\Gamma_{ad}+\partial\overline{T}/\partial z\right)/m$, where ϵ is a dimensionless factor ~1/2. By using dimensional arguments Dewan and Good (1986) predicted that the T' m-spectrum is $2\pi\left(\epsilon^2/2\right)\left(\Gamma_{ad}+\partial\overline{T}/\partial z\right)^2/m^3$ so that $\gamma\approx\epsilon^2/2\approx 1/8$.

Appendix B: Wave Diffusive Damping

Superimposed on the coherent motion of an atmospheric wave that propagates upwards are the random thermal motions of individual molecules (molecular viscosity), and the larger-scale random motions imparted by turbulence and the full spectrum of waves. The diffusion associated with these multi-scale processes degrades the organized bulk motion imparted to the atmosphere by an individual wave, and leads to attenuation of the wave. Theoretically these effects can be characterized by retaining appropriate nonlinear terms in the wave equation.

Weinstock (1982); Weinstock (1984a, 1984b, 1990) derived an expression for the nonlinear dispersion relation, which he then used to determine the growth in wave amplitude with altitude. By ignoring radiative cooling, which is negligible in the lower atmosphere below the thermosphere, and combining Weinstock's results with those of Pitteway and Hines (1963), the amplitude growth factor of a wave is

$$\exp\left[\frac{1}{2H_A}-\frac{m^3}{\omega}\left(K_{wave}+K_{zz}+\frac{K_m^m}{2}\right)\right]=\exp\left[\frac{1}{2H_A}-\frac{N^3}{k(u-c)^4}\left(K_{wave}+K_{zz}+\frac{K_m^m}{2}\right)\right] \tag{B1}$$

so that the Momentum Flux (MF) profile for an individual wave becomes

$$MF(z)=MF(z_0)\exp\left\{\int_{z_0}^{z}\left[\frac{1}{H_A}-\frac{2N^3}{k(u-c)^4}\left(K_{wave}+K_{zz}+\frac{K_m^m}{2}\right)\right]dr\right\} \tag{B2}$$

where H_A is the atmospheric density scale height, z_0 is the reference altitude near the wave source, K_m^m is the molecular viscosity which is related to the molecular diffusivity $\left(K_m^m\propto T^{2/3}/\rho_A\propto T^{1/6}K_{Mole}\right)$, m is the vertical wavenumber, k is the horizontal wave number, $c=\omega/\kappa$ is the horizontal phase velocity and u is the background wind velocity in the direction of wave propagation. Equation (B2) is identical to the expression for diffusive and radiative damping of the gravity wave stress profile derived by Garcia et al. (2007), Equation A3, for the special case where the Newtonian cooling (α) and the diffusive damping effects of waves (K_{wave}) and turbulence (K_{zz}) are ignored. Diffusive damping is most significant for short vertical wavelength, long period waves, that is waves with slow vertical phase speeds (small m/ω). Because of the dependence of K_m^m on temperature and density, damping by molecular viscosity is only important at the higher altitudes in the mesopause region and thermosphere. However, damping by waves and turbulence is important in the stratosphere and above.

Data Availability Statement

The WACCM6 model code is available for download from https://www.cesm.ucar.edu/working-groups/whole-atmosphere (WACCM, 2024). The source code of the new parametrization and the scripts used for data analysis and figures production are available from https://github.com/MariaVike/Guarino_etal_2024_JAMES (Guarino, 2024a). MIPAS data sets can be downloaded from https://earth.esa.int/eogateway/instruments/mipas (MIPAS, 2024). WACCM model outputs used to support the findings of this study are available from https://gws-access.jasmin.ac.uk/public/wavechasm/Guarino_etal_2024_JAMES (Guarino, 2024b).

Acknowledgments
M.V.G, W.F., M.M.K., D.R.M., J.M.C.P. thank the UK Natural Environment Research Council (NERC) Grant NE/T006749/1 for funding this study. W.F. acknowledges support from NERC Grant NE/P001815/1. C.S.G. acknowledges support through National Science Foundation Grants AGS 20-29162 and OPP 21-10422. B.F., M.G.C., M.L.P. acknowledge financial support from the Agencia Estatal de Investigación, MCIN/AEI/10.13039/501100011033, through Grants PID2019-110689RB-I00 and CEX2021-001131-S. The model simulations and data analysis were performed on the Leeds ARC HPC facilities.

References

Akmaev, R., & Fomichev, V. (1998). Cooling of the mesosphere and lower thermosphere due to doubling of CO_2. *Annales Geophysicae*, *16*(11), 1501–1512. https://doi.org/10.1007/s00585-998-1501-z

Becker, E., & Vadas, S. L. (2018). Secondary gravity waves in the winter mesosphere: Results from a high-resolution global circulation model. *Journal of Geophysical Research: Atmospheres*, *123*(5), 2605–2627. https://doi.org/10.1002/2017jd027460

Beres, J. H., Garcia, R. R., Boville, B. A., & Sassi, F. (2005). Implementation of a gravity wave source spectrum parameterization dependent on the properties of convection in the whole atmosphere community climate model (WACCM). *Journal of Geophysical Research*, *110*(D10). https://doi.org/10.1029/2004jd005504

Bones, D. L., Carrillo-Sánchez, J. D., Kulak, A. N., & Plane, J. M. (2019). Ablation of Ni from micrometeoroids in the upper atmosphere: Experimental and computer simulations and implications for Fe ablation. *Planetary and Space Science*, *179*, 104725. https://doi.org/10.1016/j.pss.2019.104725

Cámara, A. d. l., Lott, F., Jewtoukoff, V., Plougonven, R., & Hertzog, A. (2016). On the gravity wave forcing during the southern stratospheric final warming in LMDZ. *Journal of the Atmospheric Sciences*, *73*(8), 3213–3226. https://doi.org/10.1175/jas-d-15-0377.1

Carrillo-Sánchez, J. D., Gómez-Martín, J. C., Bones, D. L., Nesvorný, D., Pokorný, P., Benna, M., et al. (2020). Cosmic dust fluxes in the atmospheres of Earth, Mars, and Venus. *Icarus*, *335*, 113395. https://doi.org/10.1016/j.icarus.2019.113395

Carrillo-Sánchez, J. D., Nesvorný, D., Pokorný, P., Janches, D., & Plane, J. (2016). Sources of cosmic dust in the earth's atmosphere. *Geophysical Research Letters*, *43*(23), 11–979. https://doi.org/10.1002/2016gl071697

Charron, M., & Manzini, E. (2002). Gravity waves from fronts: Parameterization and middle atmosphere response in a general circulation model. *Journal of the Atmospheric Sciences*, *59*(5), 923–941. https://doi.org/10.1175/1520-0469(2002)059<0923:gwffpa>2.0.co;2

Chu, X., Gardner, C. S., Li, X., & Lin, C. Y.-T. (2022). Vertical transport of sensible heat and meteoric Na by the complete temporal spectrum of gravity waves in the MLT above McMurdo (77.84 s, 166.67 e), Antarctica. *Journal of Geophysical Research: Atmospheres*, *127*(16), e2021JD035728. https://doi.org/10.1029/2021jd035728

Colegrove, F., Hanson, W., & Johnson, F. (1965). Eddy diffusion and oxygen transport in the lower thermosphere. *Journal of Geophysical Research*, *70*(19), 4931–4941. https://doi.org/10.1029/jz070i019p04931

Coy, L., Fritts, D. C., & Weinstock, J. (1986). The stokes drift due to vertically propagating internal gravity waves in a compressible atmosphere. *Journal of the Atmospheric Sciences*, *43*(22), 2636–2643. https://doi.org/10.1175/1520-0469(1986)043<2636:tsddtv>2.0.co;2

Crutzen, P. (1970). The influence of nitrogen oxides on the atmospheric ozone content. *Quarterly Journal of the Royal Meteorological Society*, *96*(408), 320–325. https://doi.org/10.1002/qj.49709640815

Daly, S. M., Feng, W., Mangan, T. P., Gerding, M., & Plane, J. M. (2020). The meteoric Ni layer in the upper atmosphere. *Journal of Geophysical Research: Space Physics*, *125*(8), e2020JA028083. https://doi.org/10.1029/2020ja028083

Dawkins, E. C., Plane, J., Chipperfield, M., Feng, W., Marsh, D., Höffner, J., & Janches, D. (2016). Solar cycle response and long-term trends in the mesospheric metal layers. *Journal of Geophysical Research: Space Physics*, *121*(7), 7153–7165. https://doi.org/10.1002/2016ja022522

Dewan, E., & Good, R. (1986). Saturation and the "universal" spectrum for vertical profiles of horizontal scalar winds in the atmosphere. *Journal of Geophysical Research*, *91*(D2), 2742–2748. https://doi.org/10.1029/jd091id02p02742

Eckermann, S. D., Broutman, D., Ma, J., Doyle, J. D., Pautet, P.-D., Taylor, M. J., et al. (2016). Dynamics of orographic gravity waves observed in the mesosphere over the Auckland islands during the deep propagating gravity wave experiment (deepwave). *Journal of the Atmospheric Sciences*, *73*(10), 3855–3876. https://doi.org/10.1175/jas-d-16-0059.1

Ern, M., Preusse, P., Alexander, M. J., & Warner, C. D. (2004). Absolute values of gravity wave momentum flux derived from satellite data. *Journal of Geophysical Research*, *109*(D20), D20103. https://doi.org/10.1029/2004jd004752

Fan, Z., Plane, J., Gumbel, J., Stegman, J., & Llewellyn, E. (2007). Satellite measurements of the global mesospheric sodium layer. *Atmospheric Chemistry and Physics*, *7*(15), 4107–4115. https://doi.org/10.5194/acp-7-4107-2007

Feng, W., Marsh, D. R., Chipperfield, M. P., Janches, D., Höffner, J., Yi, F., & Plane, J. M. (2013). A global atmospheric model of meteoric iron. *Journal of Geophysical Research: Atmospheres*, *118*(16), 9456–9474. https://doi.org/10.1002/jgrd.50708

Fritts, D., Williams, B., She, C., Vance, J., Rapp, M., Lübken, F.-J., et al. (2004). Observations of extreme temperature and wind gradients near the summer mesopause during the MaCWAVE/MIDAS rocket campaign. *Geophysical Research Letters*, *31*(24), L24S06. https://doi.org/10.1029/2003gl019389

Funke, B., García-Comas, M., Glatthor, N., Grabowski, U., Kellmann, S., Kiefer, M., et al. (2023). Michelson interferometer for passive atmospheric sounding institute of meteorology and climate research/Instituto de Astrofísica de Andalucía version 8 retrieval of nitric oxide and lower-thermospheric temperature. *Atmospheric Measurement Techniques*, *16*(8), 2167–2196. https://doi.org/10.5194/amt-16-2167-2023

Garcia, R. R., López-Puertas, M., Funke, B., Kinnison, D. E., Marsh, D. R., & Qian, L. (2016). On the secular trend of cox and CO_2 in the lower thermosphere. *Journal of Geophysical Research: Atmospheres*, *121*(7), 3634–3644. https://doi.org/10.1002/2015jd024553

Garcia, R. R., López-Puertas, M., Funke, B., Marsh, D. R., Kinnison, D. E., Smith, A. K., & González-Galindo, F. (2014). On the distribution of CO_2 and co in the mesosphere and lower thermosphere. *Journal of Geophysical Research: Atmospheres*, *119*(9), 5700–5718. https://doi.org/10.1002/2013jd021208

Garcia, R. R., Marsh, D., Kinnison, D., Boville, B., & Sassi, F. (2007). Simulation of secular trends in the middle atmosphere, 1950–2003. *Journal of Geophysical Research*, *112*(D9), D09301. https://doi.org/10.1029/2006jd007485

Garcia, R. R., Smith, A. K., Kinnison, D. E., de la Cámara, Á., & Murphy, D. J. (2017). Modification of the gravity wave parameterization in the whole atmosphere community climate model: Motivation and results. *Journal of the Atmospheric Sciences*, *74*(1), 275–291. https://doi.org/10.1175/jas-d-16-0104.1

Garcia, R. R., & Solomon, S. (1985). The effect of breaking gravity waves on the dynamics and chemical composition of the mesosphere and lower thermosphere. *Journal of Geophysical Research*, *90*(D2), 3850–3868. https://doi.org/10.1029/jd090id02p03850

García-Comas, M., Funke, B., Gardini, A., Lopez-Puertas, M., Jurado-Navarro, A., von Clarmann, T., et al. (2014). MIPAS temperature from the stratosphere to the lower thermosphere: Comparison of vM21 with ACE-FTS, MLS, OSIRIS, SABER, SOFIE and lidar measurements. *Atmospheric Measurement Techniques*, *7*(11), 3633–3651. https://doi.org/10.5194/amt-7-3633-2014

García-Comas, M., Funke, B., López-Puertas, M., Glatthor, N., Grabowski, U., Kellmann, S., et al. (2023). Version 8 IMK–IAA MIPAS temperatures from 12–15 μ m spectra: Middle and upper atmosphere modes. *Atmospheric Measurement Techniques*, *16*(21), 5357–5386. https://doi.org/10.5194/amt-16-5357-2023

Gardner, C. S. (1996). Testing theories of atmospheric gravity wave saturation and dissipation. *Journal of Atmospheric and Terrestrial Physics*, *58*(14), 1575–1589. https://doi.org/10.1016/0021-9169(96)00027-x

Gardner, C. S. (2018). Role of wave-induced diffusion and energy flux in the vertical transport of atmospheric constituents in the mesopause region. *Journal of Geophysical Research: Atmospheres*, *123*(12), 6581–6604. https://doi.org/10.1029/2018jd028359

Gardner, C. S. (2024). Impact of atmospheric compressibility and Stokes drift on the vertical transport of heat and constituents by gravity waves. *Journal of Geophysical Research: Atmospheres*, *129*, e2023JD040436. https://doi.org/10.1029/2023JD040436

Gardner, C. S., Chu, X., Espy, P. J., Plane, J. M., Marsh, D. R., & Janches, D. (2011). Seasonal variations of the mesospheric Fe layer at Rothera, Antarctica (67.5S, 68.0W). *Journal of Geophysical Research*, *116*(D2), D02304. https://doi.org/10.1029/2010jd014655

Gardner, C. S., Guo, Y., & Liu, A. Z. (2019). Parameterizing wave-driven vertical constituent transport in the upper atmosphere. *Earth and Space Science*, *6*(6), 904–913. https://doi.org/10.1029/2019ea000625

Gardner, C. S., & Huang, W. (2016). Impact of horizontal transport, temperature, and PMC uptake on mesospheric Fe at high latitudes. *Journal of Geophysical Research: Atmospheres*, *121*(11), 6564–6580. https://doi.org/10.1002/2015jd024674

Gardner, C. S., & Liu, A. Z. (2010). Wave-induced transport of atmospheric constituents and its effect on the mesospheric Na layer. *Journal of Geophysical Research*, *115*(D20), D20302. https://doi.org/10.1029/2010jd014140

Gardner, C. S., & Liu, A. Z. (2016). Chemical transport of neutral atmospheric constituents by waves and turbulence: Theory and observations. *Journal of Geophysical Research: Atmospheres*, *121*(1), 494–520. https://doi.org/10.1002/2015jd023145

Gardner, C. S., Plane, J. M., Pan, W., Vondrak, T., Murray, B. J., & Chu, X. (2005). Seasonal variations of the Na and Fe layers at the South Pole and their implications for the chemistry and general circulation of the polar mesosphere. *Journal of Geophysical Research*, *110*(D10), D10302. https://doi.org/10.1029/2004jd005670

Gavrilov, N., Fukao, S., Nakamura, T., Tsuda, T., Yamanaka, M., & Yamamoto, M. (1996). Statistical analysis of gravity waves observed with the middle and upper atmosphere radar in the middle atmosphere: 1. Method and general characteristics. *Journal of Geophysical Research*, *101*(D23), 29511–29521. https://doi.org/10.1029/96jd01447

Gettelman, A., Mills, M., Kinnison, D., Garcia, R., Smith, A., Marsh, D., et al. (2019). The whole atmosphere community climate model version 6 (WACCM6). *Journal of Geophysical Research: Atmospheres*, *124*(23), 12380–12403. https://doi.org/10.1029/2019jd030943

Grygalashvyly, M., Becker, E., & Sonnemann, G. (2012). Gravity wave mixing and effective diffusivity for minor chemical constituents in the mesosphere/lower thermosphere. *Space Science Reviews*, *168*, 333–362. https://doi.org/10.1007/978-1-4614-5677-3_11

Guarino, M.-V. (2024a). GitHub repository. Retrieved from https://github.com/MariaVike/Guarino_etal_2024_JAMES

Guarino, M.-V. (2024b). JASMIN data. Retrieved from https://gws-access.jasmin.ac.uk/public/wavechasm/Guarino_etal_2024_JAMES

Hervig, M. E., Plane, J. M., Siskind, D. E., Feng, W., Bardeen, C. G., & Bailey, S. M. (2021). New global meteoric smoke observations from Sofie: Insight regarding chemical composition, meteoric influx, and hemispheric asymmetry. *Journal of Geophysical Research: Atmospheres*, *126*(13), e2021JD035007. https://doi.org/10.1029/2021jd035007

Hickey, M. P., Walterscheid, R. L., & Richards, P. G. (2000). Secular variations of atomic oxygen in the mesopause region induced by transient gravity wave packets. *Geophysical Research Letters*, *27*(21), 3599–3602. https://doi.org/10.1029/2000gl011953

Hines, C. O. (1960). Internal atmospheric gravity waves at ionospheric heights. *Canadian Journal of Physics*, *38*(11), 1441–1481. https://doi.org/10.1139/p60-150

Holton, J. R. (1982). The role of gravity wave induced drag and diffusion in the momentum budget of the mesosphere. *Journal of the Atmospheric Sciences*, *39*(4), 791–799. https://doi.org/10.1175/1520-0469(1982)039<0791:trogwi>2.0.co;2

Holton, J. R. (1983). The influence of gravity wave breaking on the general circulation of the middle atmosphere. *Journal of the Atmospheric Sciences*, *40*(10), 2497–2507. https://doi.org/10.1175/1520-0469(1983)040<2497:tiogwb>2.0.co;2

Holton, J. R., & Alexander, M. J. (2000). The role of waves in the transport circulation of the middle atmosphere. *Washington DC American Geophysical Union Geophysical Monograph Series*, *123*, 21–35. https://doi.org/10.1029/gm123p0021

Hu, X., Liu, A. Z., Gardner, C. S., & Swenson, G. R. (2002). Characteristics of quasi-monochromatic gravity waves observed with na lidar in the mesopause region at starfire optical range, nm. *Geophysical Research Letters*, *29*(24), 22–31. https://doi.org/10.1029/2002gl014975

Huang, W., Chu, X., Gardner, C. S., Carrillo-Sánchez, J. D., Feng, W., Plane, J. M., & Nesvorný, D. (2015). Measurements of the vertical fluxes of atomic Fe and Na at the mesopause: Implications for the velocity of cosmic dust entering the atmosphere. *Geophysical Research Letters*, *42*(1), 169–175. https://doi.org/10.1002/2014gl062390

Jiao, J., Feng, W., Wu, F., Wu, F., Zheng, H., Du, L., et al. (2022). A comparison of the midlatitude nickel and sodium layers in the mesosphere: Observations and modeling. *Journal of Geophysical Research: Space Physics*, *127*(2), e2021JA030170. https://doi.org/10.1029/2021ja030170

Jurado-Navarro, Á. A., López-Puertas, M., Funke, B., García-Comas, M., Gardini, A., González-Galindo, F., et al. (2016). Global distributions of CO_2 volume mixing ratio in the middle and upper atmosphere from daytime MIPAS high-resolution spectra. *Atmospheric Measurement Techniques*, *9*(12), 6081–6100. https://doi.org/10.5194/amt-9-6081-2016

Kiefer, M., von Clarmann, T., Funke, B., García-Comas, M., Glatthor, N., Grabowski, U., et al. (2021). IMK/IAA MIPAS temperature retrieval version 8: Nominal measurements. *Atmospheric Measurement Techniques*, *14*(6), 4111–4138. https://doi.org/10.5194/amt-14-4111-2021

Kruse, C. G., Alexander, M. J., Hoffmann, L., van Niekerk, A., Polichtchouk, I., Bacmeister, J. T., et al. (2022). Observed and modeled mountain waves from the surface to the mesosphere near the drake passage. *Journal of the Atmospheric Sciences*, *79*(4), 909–932. https://doi.org/10.1175/jas-d-21-0252.1

Lary, D. (1997). Catalytic destruction of stratospheric ozone. *Journal of Geophysical Research*, *102*(D17), 21515–21526. https://doi.org/10.1029/97jd00912

Lindzen, R. S. (1981). Turbulence and stress owing to gravity wave and tidal breakdown. *Journal of Geophysical Research*, *86*(C10), 9707–9714. https://doi.org/10.1029/jc086ic10p09707

Liu, A. Z., & Gardner, C. S. (2004). Vertical dynamical transport of mesospheric constituents by dissipating gravity waves. *Journal of Atmospheric and Solar-Terrestrial Physics*, *66*(3–4), 267–275. https://doi.org/10.1016/j.jastp.2003.11.002

Liu, A. Z., & Gardner, C. S. (2005). Vertical heat and constituent transport in the mesopause region by dissipating gravity waves at Maui, Hawaii (20.7 N), and starfire optical range, New Mexico (35 N). *Journal of Geophysical Research*, *110*(D9), D09S13. https://doi.org/10.1029/2004jd004965

Liu, H. L. (2019). Quantifying gravity wave forcing using scale invariance. *Nature Communications*, *10*(1), 1–12. https://doi.org/10.1038/s41467-019-10527-z

López-Puertas, M., Funke, B., Jurado-Navarro, Á., García-Comas, M., Gardini, A., Boone, C., et al. (2017). Validation of the mipas CO_2 volume mixing ratio in the mesosphere and lower thermosphere and comparison with WACCM simulations. *Journal of Geophysical Research: Atmospheres*, *122*(15), 8345–8366. https://doi.org/10.1002/2017jd026805

López-Puertas, M., & Taylor, F. W. (2001). *Non-LTE radiative transfer in the atmosphere* (Vol. 3). World Scientific. https://doi.org/10.1142/9789812811493

Marsh, D. R., Janches, D., Feng, W., & Plane, J. M. (2013). A global model of meteoric sodium. *Journal of Geophysical Research: Atmospheres*, *118*(19), 11–442. https://doi.org/10.1002/jgrd.50870

Matsuno, T. (1982). A quasi one-dimensional model of the middle atmosphere circulation interacting with internal gravity waves. *Journal of the Meteorological Society of Japan. Ser. II*, *60*(1), 215–226. https://doi.org/10.2151/jmsj1965.60.1_215

McFarlane, N. (1987). The effect of orographically excited gravity wave drag on the general circulation of the lower stratosphere and troposphere. *Journal of the Atmospheric Sciences*, *44*(14), 1775–1800. https://doi.org/10.1175/1520-0469(1987)044<1775:teooeg>2.0.co;2

McLandress, C. (1997). Sensitivity studies using the Hines and Fritts gravity wave drag parameterizations. In *Gravity wave processes: Their parameterization in global climate models* (pp. 245–255).

McLandress, C., Shepherd, T. G., Polavarapu, S., & Beagley, S. R. (2012). Is missing orographic gravity wave drag near 60° s the cause of the stratospheric zonal wind biases in chemistry–climate models? *Journal of the Atmospheric Sciences*, *69*(3), 802–818. https://doi.org/10.1175/jas-d-11-0159.1

MIPAS. (2024). Dataset. Retrieved from https://earth.esa.int/eogateway/instruments/mipas

Nesvornỳ, D., Janches, D., Vokrouhlickỳ, D., Pokornỳ, P., Bottke, W. F., & Jenniskens, P. (2011). Dynamical model for the zodiacal cloud and sporadic meteors. *The Astrophysical Journal*, *743*(2), 129. https://doi.org/10.1088/0004-637x/743/2/129

Pitteway, M., & Hines, C. (1963). The viscous damping of atmospheric gravity waves. *Canadian Journal of Physics*, *41*(12), 1935–1948. https://doi.org/10.1139/p63-194

Plane, J. M. (2012). Cosmic dust in the Earth's atmosphere. *Chemical Society Reviews*, *41*(19), 6507–6518. https://doi.org/10.1039/c2cs35132c

Plane, J. M., Feng, W., & Dawkins, E. C. (2015). The mesosphere and metals: Chemistry and changes. *Chemical Reviews*, *115*(10), 4497–4541. https://doi.org/10.1021/cr500501m

Plane, J. M., Murray, B. J., Chu, X., & Gardner, C. S. (2004). Removal of meteoric iron on polar mesospheric clouds. *Science*, *304*(5669), 426–428. https://doi.org/10.1126/science.1093236

Portmann, R., Thomas, G., Solomon, S., & Garcia, R. (1995). The importance of dynamical feedbacks on doubled co2-induced changes in the thermal structure of the mesosphere. *Geophysical Research Letters*, *22*(13), 1733–1736. https://doi.org/10.1029/95gl01432

Richter, J. H., Sassi, F., & Garcia, R. R. (2010). Toward a physically based gravity wave source parameterization in a general circulation model. *Journal of the Atmospheric Sciences*, *67*(1), 136–156. https://doi.org/10.1175/2009jas3112.1

Shepherd, G. G., Liu, G., & Roble, R. G. (2004). Remote sensing of the large-scale circulation of atomic oxygen. *Remote sensing of clouds and the atmosphere ix*, *5571*, 173–181. https://doi.org/10.1117/12.567886

Smith, A. K., Marsh, D. R., Mlynczak, M. G., & Mast, J. C. (2010). Temporal variations of atomic oxygen in the upper mesosphere from saber. *Journal of Geophysical Research*, *115*(D18), D18309. https://doi.org/10.1029/2009jd013434

States, R. J., & Gardner, C. S. (1999). Structure of the mesospheric Na layer at 40° N latitude: Seasonal and diurnal variations. *Journal of Geophysical Research*, *104*(D9), 11783–11798. https://doi.org/10.1029/1999jd900002

Strelnikova, I., Baumgarten, G., & Lübken, F.-J. (2020). Advanced hodograph-based analysis technique to derive gravity-wave parameters from lidar observations. *Atmospheric Measurement Techniques*, *13*(2), 479–499. https://doi.org/10.5194/amt-13-479-2020

VanZandt, T. E., & Fritts, D. C. (1989). A theory of enhanced saturation of the gravity wave spectrum due to increases in atmospheric stability (pp. 399–420).

WACCM. (2024). Model source code. Retrieved from https://www.cesm.ucar.edu/working-groups/whole-atmosphere

Walterscheid, R., & Hickey, M. (2009). Gravity wave ducting in the upper mesosphere and lower thermosphere duct system. *Journal of Geophysical Research*, *114*(D19), D19109. https://doi.org/10.1029/2008jd011269

Walterscheid, R., & Hocking, W. (1991). Stokes diffusion by atmospheric internal gravity waves. *Journal of the Atmospheric Sciences*, *48*(20), 2213–2230. https://doi.org/10.1175/1520-0469(1991)048<2213:sdbaig>2.0.co;2

Walterscheid, R., & Schubert, G. (1989). Gravity wave fluxes of O_3 and oh at the nightside mesopause. *Geophysical Research Letters*, *16*(7), 719–722. https://doi.org/10.1029/gl016i007p00719

Wang, L., Geller, M. A., & Alexander, M. J. (2005). Spatial and temporal variations of gravity wave parameters. part i: Intrinsic frequency, wavelength, and vertical propagation direction. *Journal of the Atmospheric Sciences*, *62*(1), 125–142. https://doi.org/10.1175/jas-3364.1

Ward, W. (1999). A simple model of diurnal variations in the mesospheric oxygen nightglow. *Geophysical Research Letters*, *26*(23), 3565–3568. https://doi.org/10.1029/1999gl003661

Weinstock, J. (1976). Nonlinear theory of acoustic-gravity waves 1. saturation and enhanced diffusion. *Journal of Geophysical Research*, *81*(4), 633–652. https://doi.org/10.1029/ja081i004p00633

Weinstock, J. (1982). Nonlinear theory of gravity waves: Momentum deposition, generalized Rayleigh friction, and diffusion. *Journal of the Atmospheric Sciences*, *39*(8), 1698–1710. https://doi.org/10.1175/1520-0469(1982)039<1698:ntogwm>2.0.co;2

Weinstock, J. (1984a). Gravity wave saturation and eddy diffusion in the middle atmosphere. *Journal of Atmospheric and Terrestrial Physics*, *46*(11), 1069–1082. https://doi.org/10.1016/0021-9169(84)90009-6

Weinstock, J. (1984b). Simplified derivation of an algorithm for nonlinear gravity waves. *Journal of Geophysical Research*, *89*(A1), 345–350. https://doi.org/10.1029/ja089ia01p00345

Weinstock, J. (1990). Saturated and unsaturated spectra of gravity waves and scale-dependent diffusion. *Journal of the Atmospheric Sciences*, *47*(18), 2211–2226. https://doi.org/10.1175/1520-0469(1990)047<2211:sausog>2.0.co;2

Whiteway, J. A. (1999). Enhanced and inhibited gravity wave spectra. *Journal of the Atmospheric Sciences*, *56*(10), 1344–1352. https://doi.org/10.1175/1520-0469(1999)056<1344:eaigws>2.0.co;2

Yu, B., Xue, X., Scott, C. J., Jia, M., Feng, W., Plane, J., et al. (2022). Comparison of middle-and low-latitude sodium layer from a ground-based lidar network, the Odin satellite, and WACCM–Na model. *Atmospheric Chemistry and Physics*, *22*(17), 11485–11504. https://doi.org/10.5194/acp-22-11485-2022

Yu, Y., & Hickey, M. P. (2007). Numerical modeling of a gravity wave packet ducted by the thermal structure of the atmosphere. *Journal of Geophysical Research*, *112*(A6), A06308. https://doi.org/10.1029/2006ja012092